

Abstract

Seismic interferometry is a powerful tool to monitor the seismic velocity change associated with volcanic eruptions. For the monitoring, changes in seismic velocity with environmental origins (such as precipitation) are problematic. In order to model the environmental effects, we propose a new technique based on a state-space model. An extended Kalman filter estimates seismic velocity changes as state variables, with a first-order approximation of the stretching method. We apply this technique to three-component seismic records in order to detect the seismic velocity change associated with the Shinmoe-dake eruptions in 2011 and 2018. First, ambient noise cross-correlations were calculated from May 2010 to April 2018. We also modeled seismic velocity changes resulting from precipitation and the 2016 Kumamoto earthquake, with exponential type responses. Most of the results show no significant changes associated with the eruptions, although gradual inflation of the magma reservoir preceded the 2011 eruption by one year. The observed low sensitivity to static stress changes suggests that the fraction of geofluid and crack density at about 1 km depth is small, and the crack shapes could be circular. Only one station pair west of the crater shows the significant drop associated with the eruption in 2011. The gradual drop of seismic velocity up to 0.05% preceded the eruption by one month. When the gradual drop began, volcanic tremors were activated at about 2 km depth. These observations suggest that the drop could be caused by damage accumulation due to vertical magma migration beneath the summit.

1 Introduction

Shinmoe-dake forms part of a group of Kirishima volcanoes, located in Kyusyu Japan, and is an active volcano. Over a period of ten years, it experienced a major eruption in 2011, and a effusive eruption in 2018. In 2011, the eruptive sequence started with sub-Plinian eruptions (January 26-27th), followed by a lava effusion (January 28-31st), and culminating in Vulcanian eruptions (1-10 Feb.) (Nakada et al., 2013). Observations from Global Navigation Satellite Systems (GNSS) show that the gradual inflation of the magma reservoir preceded the 2011 eruption by one year. The magma reservoir is located approximately 7 km northwest of Shinmoe-dake at a depth of approximately 8 km below sea level (BSL) (Nakao et al., 2013; Kozono et al., 2013). When the inflation started, low-frequency earthquakes (LFE) at a depth of 20-27 km was activated, suggesting the migration of magma from a deeper region (Kurihara et al., 2019). During the 2011 eruptions, the GNSS data indicate the co-eruption deflation of the magma reservoir. Tilt observation showed an-hour-long inflation and rapid deflation at a shallow depth (around 500 m) near the summit right before the first sub-Plinian event (Takeo et al., 2013). Also stepwise local tilt inflations were reported twice in about a week before the sub-Plinian event (Ichihara & Matsumoto, 2017). During the eruption, explosion earthquakes were observed (Nakamichi et al., 2013). The activities suggest that the magma touched an aquifer at shallow depths of about -1.0 km BSL (e.g., Kagiya et al., 1996). Before and during the sub-Plinian eruptions, migration of gas (probably with magma) also activated continuous volcanic tremors (Ichihara & Matsumoto, 2017). These were located beneath the crater for one week before the major eruption, and they rose from a depth of a few kilometers to the near-surface aquifer three times. The heat transported to the water layer could have triggered the sub-Plinian eruptions (Ichihara & Matsumoto, 2017). In order to understand the magma plumping system, pertinent information from depths of 1 to 10 km is crucial. However, we could not detect earthquake activity at these depths before the major eruptions associated with the magma migration (Ueda et al., 2013) and other geophysical phenomena.

Seismic interferometry is a powerful technique for monitoring seismic velocity in the depth range of interest. In recent years, the number of applications of seismic interferometry has increased. In the analysis, the cross-correlation function between ambient noise records of a pair of stations can be regarded as a virtual seismic waveform, recorded

at one station when the source is placed at the other station. In any time period, the seismic velocity around the station pair can be estimated from the cross-correlation function calculated without an earthquake; thus, seismic interferometry has been applied in many studies to monitor temporal changes in seismic velocity (e.g., Obermann & Hillers, 2019). This technique has been applied for detecting seismic wave velocity changes after large earthquakes (e.g., Wegler & Sens-Schönfelder, 2007; Wegler et al., 2009; Brenguier, Campillo, et al., 2008; Brenguier et al., 2014), those of a slow slip event (Rivet et al., 2011), and those associated with volcanic eruptions: e.g., the Piton de La Fournaise volcano, La Réunion, France (Brenguier, Shapiro, et al., 2008), Mt. Asama, Japan (Nagaoka et al., 2010), Merapi volcano, Indonesia (Budi-Santoso & Lesage, 2016), Ubinas volcano, Peru (Machacca et al., 2019), and Kilauea volcano, USA (Donaldson et al., 2017). For example, Brenguier, Shapiro, et al. (2008) detected a drop in seismic velocity of the order of 0.1% for a number of days preceding the eruption of the Piton de La Fournaise volcano, and the velocity recovered at a time scale of about 10-20 days. There are two potential mechanisms for the temporal changes (Olivier et al., 2019). The first is pressurization due to the magma migration in a linear elastic regime. In this regime, stress sensitivity of seismic velocity change is a proxy for inferring the state of the material: in particular the existence of geofluid (Brenguier et al., 2014). The second is damage accumulation beyond the linear elastic regime.

The biggest technical difficulty in monitoring is the separation of temporal variations of volcanic origin from environmental variations. Many researchers reported seasonal variations associated with environmental phenomena: rainfall (e.g., Rivet et al., 2015), air pressure (e.g., Niu et al., 2008), and thermo-elasticity (e.g., Hillers, Ben-Zion, et al., 2015). In the region of Mt. Shimoe-dake, daily precipitation exceeds 100 mm for several days in a year, while the annual precipitation is more than 4000 mm. Wang et al. (2017) reported that rainfall is the major source of the observed temporal changes in this area (Kyusyu). The Merapi Volcano, Indonesia, Sens-Schönfelder and Wegler (2006) also experienced the observed dominance of seasonal variations. Temporal changes in groundwater levels based on precipitation data can explain the observed strong seasonal variations in both cases. Such strong seasonal variations have the potential to mask a temporal change associated with volcanic activities; thus, correction for rainfall is crucial for inferring the temporal changes associated with volcanic activity (Rivet et al., 2015; Wang et al., 2017).

Earthquakes also contaminate temporal changes in seismic velocities associated with volcanic activities. In particular, this region experienced the 2016 Kumamoto earthquake of Mw 7.3 (e.g., Kato et al., 2016). The seismic-velocity dropped during the earthquake, and recovered over a time scale of several months (Nimiya et al., 2017). Since the seismic-velocity reduction on the order of 0.1% could be comparable to typical temporal variations associated with volcanic activities, it should be subtracted. Moreover, the susceptibility, which is defined by the ratio between observed reductions in seismic velocity and the estimated dynamic stress (Brenguier et al., 2014), is a good proxy for discussing the state of geofluid in the upper crust associated with a volcanic process.

In this study, we introduce an empirical Bayes approach to separate the effects of precipitation and the earthquake from the observed seismic velocity changes to extract those of volcanic origins (Malinverno & Briggs, 2004). It has two levels of inference. At the lower level, the seismic velocity changes were modeled in a state-space form. An extended Kalman filter/smoothing (section 4) estimates seismic velocity changes as state variables. Precipitation and earthquake effects are modeled as explanatory variables, which are deterministic at this level. At the higher level, hyper-parameters (model covariance, data covariance, and explanatory variables) are estimated by the Maximum Likelihood Method (section 5). This two-level approach has the following features: (1) we can constrain the hyper-parameters from data directly. (2) we can evaluate the separation of the origins in a statistical manner, (3) the approach gives us a criterion of the model selec-

119 tion (see section 5.3 for details) and (4) the extended Kalman filter/smoothing is numerically efficient. Notation section at the end of this paper provides a list of definitions of the variables used in this paper.

122 We combine the extracted temporal velocity changes of volcanic origins with the geodetic observation and volcanic tremor activity to discuss the magma migration in section 6.

125 2 Cross-correlation analysis

126 We used three component seismograms recorded at eight stations (six broadband sensors and two short-period sensors with a natural frequency of 1 Hz) from May 1st, 2010 to April 30th, 2018, shown in Figure 1. Five stations were deployed by the Earthquake Research Institute, the University of Tokyo, and the other three were deployed by the National Research Institute for Earth Science and Disaster Prevention (NIED). The details of the sensors are shown in Table 1. We used daily precipitation data recorded by a station (Ebino shown by the white circle in Figure 1) of the Japan Meteorological Agency (JMA) for correcting the precipitation effects as described in section 5.1.

134 First, the data were down-sampled from 100 Hz to 2.5 Hz. The instrumental responses were corrected in time domain (Maeda et al., 2011) according to the sensor type, and all records were bandpass-filtered from 0.15 to 0.90 Hz. For each station pair, the two horizontal components were rotated into radial and transverse coordinates according to the geometry of the station pair: the radial direction is parallel to the great circle path between the station pair, and the transverse direction is perpendicular to the great circle path (Nishida et al., 2008). The daily records were divided into segments of 409.6 s, with an overlap of 204.8 s.

142 To reject noisy data, which include transient phenomena such as high instrumental noise or earthquakes, we discarded the noisy segments as follows. For one-day data of each component at a station, we estimated the root mean squared amplitudes (RMSs) of all the segments. For each component of one-day data, we defined the threshold to be twice the median value of RMSs for all the segments in one day. If the RMS of a segment was larger than the threshold, the segment was discarded.

Network	Station name	Sensor type
ERI	KVO	L4-C (1 s, -2/2/2011), Trillium-120 (120 s, 2/3/2011-)
ERI	SMN	Trillium-40 (40 s, -7/22/2010) Trillium-120 (120 s, 7/23/2010-)
ERI	SMW	L4-C (1 s)
ERI	TKW	CMG3T (100 s)
ERI	TKS	Trillium-40 (40 s, -2/4/2011) Trillium-120 (120 s, 2/5/2011-)
NIED (V-net)	KRHV	Trillium-240 (240 s)
NIED (V-net)	KRMV	Trillium-240 (240 s)
NIED (Hi-net)	MJNH	Hi-net 1 Hz velocity meter (1 s)

Table 1. Sensor type for each station. ERI represents a station deployed by the Volcano Research Center, Earthquake Research Institute, the University of Tokyo. NIED (V-net) means a station of the Volcano Observation network deployed by the National Research Institute for Earth Science and Disaster Prevention, and NIED (Hi-net) means a station of High-Sensitivity Seismograph Network deployed by NIED.

148 We then took cross-correlation functions (CCFs) of all possible pairs of stations, and all possible component combinations for each station pair with the spectral whiten-

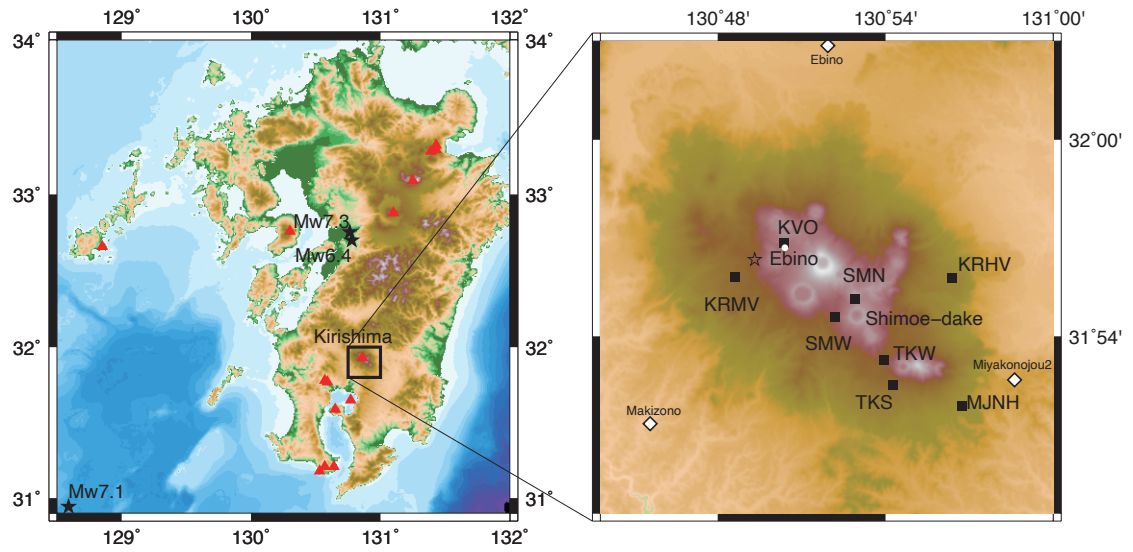


Figure 1. Left: Location of the Kirishima volcanic group. Red triangles show active volcanoes. Black stars represent the hypocenters of earthquakes: (i) Mw 6.4, April 14th (UTC), 2016, the foreshock of the Kumamoto earthquake, (ii) Mw 7.3, April 15th (UTC), 2016, the mainshock of the Kumamoto earthquake and (ii) Mw 7.1, November 13th (UTC), 2015, the Satsuma earthquake. Right: Station distribution. Black squares show station locations, and the white circle shows the JMA weather station. Three white diamond symbols show the locations of GEONET stations operated by the Geospatial Information Authority of Japan. The star symbol shows the location of a volumetric source at a depth of 8.35 km (Nakao et al., 2013). The topography in the right panel is given by the corresponding Shuttle Radar Topography Mission (Farr et al., 2007).

150 ing, as done in previous studies (Bensen et al., 2007). We stacked the CCFs of the se-
 151 lected segments over one day. The daily CCFs of the individual pairs of stations were
 152 represented by $\phi_t^p(\tau)$, where τ shows lag time, and the subscript t is an integer, which
 153 represents days from 1 May 2010 (JST), and the superscript p shows the pair of compo-
 154 nents (9 components: $R-R$, $R-T$, ..., $Z-Z$, where R is the radial component,
 155 and T is transverse component, and Z is vertical component). Figure 2 shows a typi-
 156 cal example of daily CCFs, which are stable even in their coda parts for eight years. Fig-
 157 ure 3 shows a typical example of the mean power spectrum of the mean CCF between
 158 a pair of broadband stations, which shows dominance in lower frequencies from 0.25-0.5
 159 Hz, even after the spectral whitening.

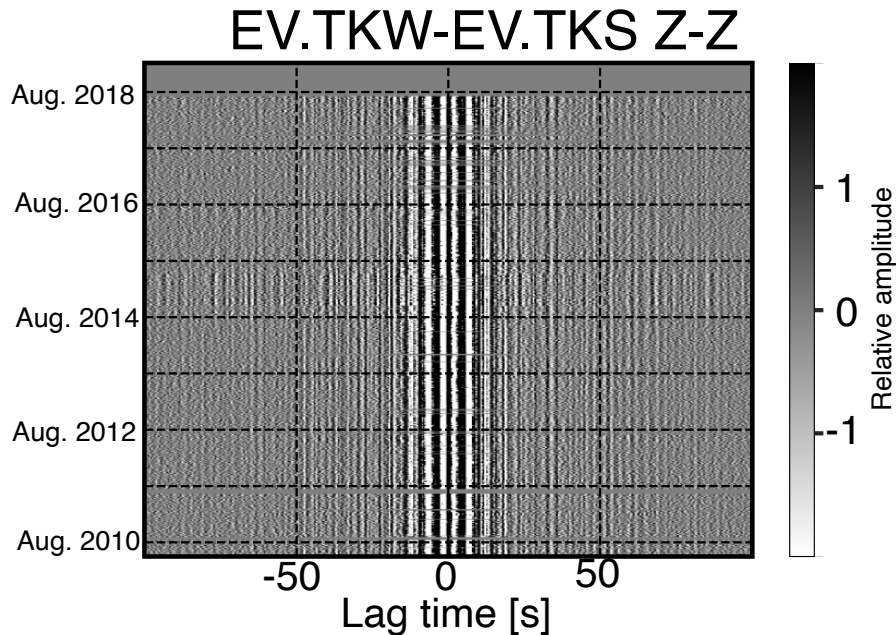


Figure 2. Daily CCFs of Z-Z component (0.2-0.4 Hz) between TKS and TKW. The vertical axis shows date, the horizontal axis shows lag time.

160 3 Measurements of seismic velocity change

161 Seismic interferometry is feasible for monitoring seismic wave velocity between pairs
 162 of stations. The principle of seismic interferometry is that the CCF between a station
 163 pair represents the seismic wavefield as though a source lies at one station and a receiver
 164 lies at the other. However, the disadvantage of this technique is that the measurements
 165 are overly sensitive to source heterogeneity (e.g., Weaver et al., 2009). This causes a trade-
 166 off between a temporal change of seismic velocity and that of source heterogeneity. Al-
 167 though the direct waves are sensitive to the source heterogeneity, the coda part becomes
 168 insensitive with increasing lapse time. This is because the seismic wavefield loses the source
 169 information over multiple scatterings (Colombi et al., 2014). If the seismic velocity changes
 170 uniformly in space, the arrival time delays with lapse time. This approach is known as
 171 the doublet method in frequency domain, first applied to earthquake coda (Poupinet et
 172 al., 1984). This method is also feasible for monitoring of seismic velocity with seismic
 173 interferometry (e.g., Brenguier et al., 2014; Hillers, Husen, et al., 2015). We used the method
 174 in the time domain, known as the stretching method (Weaver & Lobkis, 2000), because

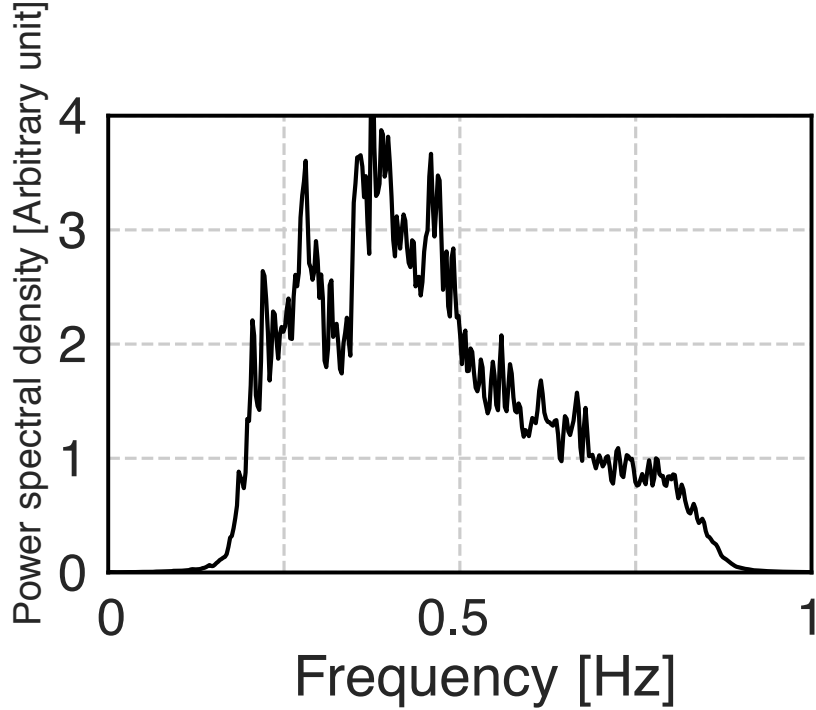


Figure 3. Power spectrum averaged over all CCFs between TKS and TKW with the time window from -99.6 to -20 s and from 20 to 99.6 s.

175 the linearization is easier for an application of an extended Kalman filter as described
 176 in the next section.

177 We constructed a model function, $m^p(A_t, \gamma_t; \tau)$, for the observed CCF $\phi_t^p(\tau)$ by stretch-
 178 ing the reference CCF $\varphi_{ref}^p(\tau)$ as,

$$179 \quad m^p(A_t, \gamma_t; \tau) = A_t \varphi_{ref}^p(\tau(1 + \gamma_t)), \quad (1)$$

180 where γ_t is the stretching factor, A_t is amplitude and the subscript t represents day. The
 181 initial reference CCF $\varphi_{ref}^p(\tau)$ was estimated by averaging all the observed CCFs $\phi_t^p(\tau)$
 182 over days t (see section 4.1).

183 To estimate the temporal evolution of γ_t , Weaver and Lobkis (2000) constructed
 184 a dilation correlation coefficient between waveforms X^p as,

$$185 \quad X^p(\gamma_t) = \frac{\int \phi_t^p(\tau) m^p(A_t, \gamma_t; \tau) d\tau}{\sqrt{\int \phi_t^p(\tau)^2 d\tau} \sqrt{\int (m^p(A_t, \gamma_t; \tau))^2 d\tau}}. \quad (2)$$

186 By maximizing the correlation, the temporal variation γ_t can be estimated. Several re-
 187 searchers have used this method to measure the temporal changes in seismic velocity.
 188 To enhance the signal to noise ratio, measurements over many station pairs and com-
 189 ponents were averaged. Bayesian approaches (e.g., Tarantola & Valette, 1982) for these
 190 measurements are feasible for more reliable estimations (Breguier et al., 2016).

191 To enhance the flexibility of the Bayesian approach, we developed a new method
 192 of an extended Kalman filter based on the state-space model (e.g., Segall & Matthews,
 193 1997; Durbin & Koopman, 2012). This method, successively, minimizes the squared dif-
 194 ference given by

$$195 \quad S(A_t, \gamma_t) \equiv \int (\phi_t^p(\tau) - m^p(A_t, \gamma_t; \tau))^2 d\tau. \quad (3)$$

196 A_t and γ_t are recognized as state variables for the state modeling as shown in the next
 197 section.

198 In sections 4 and 5, we introduce an empirical Bayes approach to minimize the squared
 199 difference. It has two levels of inference. At the lower level, the seismic velocity changes
 200 were modeled in a state-space form. An extended Kalman filter/smoothing (section 4)
 201 estimates seismic velocity changes as state variables. At the higher level, hyper-parameters
 202 (model covariance, data covariance, and explanatory variables for precipitation and earth-
 203 quake effects) are estimated by the Maximum Likelihood Method (section 5).

204 4 State Space modeling using an extended Kalman filter approach

205 Here we considered state variables α_t , which describe the amplitude A_t and the
 206 stretching factor γ_t at $t = 1, \dots, n$ assuming that the state variables are common to
 207 all the 9 components for each station pair. The state variables and the data vector of
 208 observed CCF \mathbf{y}_t^p for a p th component are defined by

$$209 \quad \alpha_t \equiv \begin{pmatrix} A_t \\ \gamma_t \end{pmatrix}, \mathbf{y}_t^p \equiv \begin{pmatrix} \phi_t^p(-\tau_e) \\ \vdots \\ \phi_t^p(-\tau_s) \\ \phi_t^p(\tau_s) \\ \vdots \\ \phi_t^p(\tau_e) \end{pmatrix}, \quad (4)$$

210 where τ_s is the start of lag time (20 s) and τ_e is the end of lag time (99.6 s). They obey
 211 the following relations:

$$212 \quad \mathbf{y}_t^p = \mathbf{m}^p(\alpha_t + \mathbf{R}_t + \mathbf{E}_t) + \epsilon_t, \quad \epsilon_t \sim \mathcal{N}(0, \mathbf{H}_t) \quad (5)$$

$$213 \quad \alpha_{t+1} = \alpha_t + \boldsymbol{\eta}_t, \quad \boldsymbol{\eta}_t \sim \mathcal{N}(0, \mathbf{Q}_t). \quad (6)$$

215 Here we introduce explanatory variables \mathbf{R}_t related to precipitation (Wang et al., 2017)
 216 and \mathbf{E}_t associated with the seismic-velocity drop during the 2016 Kumamoto earthquake
 217 (Nimiya et al., 2017), respectively. Because the explanatory variables are recognized as
 218 hyper-parameters in this study, they are deterministic at this level. Subsequently, they
 219 are estimated by Maximum Likelihood Method at the higher level (see section 5 for details).
 220 Section 5.3 also shows how to choose explanatory variables based on likelihood.
 221 ϵ_t and $\boldsymbol{\eta}_t$ are mutually independent random variables, subject to normal distribution (\mathcal{N})
 222 with zero means and covariance matrix \mathbf{H}_t and \mathbf{Q}_t , respectively. The model \mathbf{m}^p are defined by
 223

$$224 \quad \mathbf{m}^p(\alpha_t + \mathbf{R}_t + \mathbf{E}_t) \equiv \begin{pmatrix} m^p(\alpha_t + \mathbf{R}_t + \mathbf{E}_t; -\tau_e) \\ \vdots \\ m^p(\alpha_t + \mathbf{R}_t + \mathbf{E}_t; -\tau_s) \\ m^p(\alpha_t + \mathbf{R}_t + \mathbf{E}_t; \tau_s) \\ \vdots \\ m^p(\alpha_t + \mathbf{R}_t + \mathbf{E}_t; \tau_e) \end{pmatrix}. \quad (7)$$

225 Since the sampling interval of CCFs is 0.4 s, the dimension of the vectors \mathbf{y}_t^p and \mathbf{m}^p is
 226 $2 \cdot ((\tau_e - \tau_s)/0.4 + 1) = 400$. With an assumption of the constant data covariance with
 227 respect to time and lag time, \mathbf{H}_t can be written by a diagonal matrix:

$$228 \quad \mathbf{H}_t \equiv h_0 \mathbf{I}, \quad (8)$$

229 where h_0 is a prior data covariance and \mathbf{I} is the 400×400 identity matrix. Assuming
 230 that the amplitude A_t does not correlate with the seismic velocity change γ_t , we can write
 231 \mathbf{Q}_t as a diagonal matrix:

$$232 \quad \mathbf{Q}_t \equiv \begin{pmatrix} q_0 & 0 \\ 0 & q_1 \end{pmatrix}, \quad (9)$$

233 where q_0 and q_1 are a prior model covariance. h_0 is estimated from the time average of
 234 the squared difference between $\phi_t^p(\tau)$ and the reference $\varphi_{ref}^p(\tau)$. Since the amplitude A_t
 235 is a kind of normalization factor, it is difficult to separate the origins: volcanic, precipi-
 236 tation, or earthquake. For simplicity, we omitted the amplitude term A_t for precipita-
 237 tion and earthquakes. Accordingly \mathbf{R}_t and \mathbf{E}_t are given by,

$$238 \quad \mathbf{R}_t \equiv \begin{pmatrix} 0 \\ r_t \end{pmatrix}, \mathbf{E}_t \equiv \begin{pmatrix} 0 \\ e_t \end{pmatrix}. \quad (10)$$

239 The state variable $\boldsymbol{\alpha}_t$ has an initial value \mathbf{a}_1 at $t = 1$ subject to a normal distri-
 240 bution $\sim N(\mathbf{a}_1, \mathbf{P}_1)$ defined by

$$241 \quad \mathbf{a}_1 \equiv \begin{pmatrix} A_1 \\ \gamma_1 \end{pmatrix}, \mathbf{P}_1 \equiv \begin{pmatrix} p_0 & 0 \\ 0 & p_1 \end{pmatrix}, \quad (11)$$

242 where A_1 is a prior initial amplitude, γ_1 is a prior initial stretching factor, p_0 and p_1 are
 243 a prior model covariance for the initial value. First, we assumed that \mathbf{Q}_t , \mathbf{R}_t , \mathbf{E}_t and \mathbf{P}_1
 244 are given in advance; that is, they are recognized as hyper-parameters.

245 We linearized equation (1) (e.g., Weaver et al., 2011) in order to apply the extended
 246 Kalman filter. We consider the update of state variable from the initial guess $\hat{\boldsymbol{\alpha}}_t \equiv (\hat{A}_t, \hat{\gamma}_t)^T$.
 247 Assuming that the increment from the initial guess $\Delta\boldsymbol{\alpha}$ is small, Taylor series of \mathbf{m}^p in
 248 equation (5) at around the initial guess $\hat{\boldsymbol{\alpha}}_t$ up to 1st order lead the following equation,

$$249 \quad \mathbf{m}^p(\hat{\boldsymbol{\alpha}}_t + \Delta\boldsymbol{\alpha} + \mathbf{R}_t + \mathbf{E}_t) = \mathbf{m}^p(\hat{\boldsymbol{\alpha}}_t + \mathbf{R}_t + \mathbf{E}_t) + \boldsymbol{\zeta}_t^p \Delta\boldsymbol{\alpha}, \quad (12)$$

250 where

$$251 \quad \boldsymbol{\zeta}_t^p = \begin{pmatrix} \varphi_{ref}^p(-(1 + \hat{\gamma}_t + r_t + e_t)\tau_e) & -\hat{A}_t \tau_e \dot{\varphi}_{ref}^p(-(1 + \hat{\gamma}_t + r_t + e_t)\tau_e) \\ \vdots & \vdots \\ \varphi_{ref}^p(-(1 + \hat{\gamma}_t + r_t + e_t)\tau_s) & -\hat{A}_t \tau_s \dot{\varphi}_{ref}^p(-(1 + \hat{\gamma}_t + r_t + e_t)\tau_s) \\ \varphi_{ref}^p((1 + \hat{\gamma}_t + r_t + e_t)\tau_s) & \hat{A}_t \tau_s \dot{\varphi}_{ref}^p((1 + \hat{\gamma}_t + r_t + e_t)\tau_s) \\ \vdots & \vdots \\ \varphi_{ref}^p((1 + \hat{\gamma}_t + r_t + e_t)\tau_e) & \hat{A}_t \tau_e \dot{\varphi}_{ref}^p((1 + \hat{\gamma}_t + r_t + e_t)\tau_e) \end{pmatrix}, \quad (13)$$

252 and $\dot{\varphi}$ represents the derivative of φ .

253 Since nine components of the cross-correlation functions were used in this study,
 254 we define the following vectors:

$$255 \quad \mathbf{Y}_t \equiv \begin{pmatrix} \mathbf{y}_t^{RR} \\ \mathbf{y}_t^{RT} \\ \mathbf{y}_t^{RZ} \\ \mathbf{y}_t^{TR} \\ \mathbf{y}_t^{TT} \\ \mathbf{y}_t^{TZ} \\ \mathbf{y}_t^{ZR} \\ \mathbf{y}_t^{ZT} \\ \mathbf{y}_t^{ZZ} \end{pmatrix}, \mathbf{Z}_t(\hat{\boldsymbol{\alpha}}_t) \equiv \begin{pmatrix} \boldsymbol{\zeta}_t^{RR} \\ \boldsymbol{\zeta}_t^{RT} \\ \boldsymbol{\zeta}_t^{RZ} \\ \boldsymbol{\zeta}_t^{TR} \\ \boldsymbol{\zeta}_t^{TT} \\ \boldsymbol{\zeta}_t^{TZ} \\ \boldsymbol{\zeta}_t^{ZR} \\ \boldsymbol{\zeta}_t^{ZT} \\ \boldsymbol{\zeta}_t^{ZZ} \end{pmatrix}, \mathbf{M}_t(\hat{\boldsymbol{\alpha}}_t) \equiv \begin{pmatrix} \mathbf{m}^{RR}(\hat{\boldsymbol{\alpha}}_t + \mathbf{R}_t + \mathbf{E}_t) \\ \mathbf{m}^{RT}(\hat{\boldsymbol{\alpha}}_t + \mathbf{R}_t + \mathbf{E}_t) \\ \mathbf{m}^{RZ}(\hat{\boldsymbol{\alpha}}_t + \mathbf{R}_t + \mathbf{E}_t) \\ \mathbf{m}^{TR}(\hat{\boldsymbol{\alpha}}_t + \mathbf{R}_t + \mathbf{E}_t) \\ \mathbf{m}^{TT}(\hat{\boldsymbol{\alpha}}_t + \mathbf{R}_t + \mathbf{E}_t) \\ \mathbf{m}^{TZ}(\hat{\boldsymbol{\alpha}}_t + \mathbf{R}_t + \mathbf{E}_t) \\ \mathbf{m}^{ZR}(\hat{\boldsymbol{\alpha}}_t + \mathbf{R}_t + \mathbf{E}_t) \\ \mathbf{m}^{ZT}(\hat{\boldsymbol{\alpha}}_t + \mathbf{R}_t + \mathbf{E}_t) \\ \mathbf{m}^{ZZ}(\hat{\boldsymbol{\alpha}}_t + \mathbf{R}_t + \mathbf{E}_t) \end{pmatrix} \quad (14)$$

256 4.1 Calculation of the reference CCF

257 First, we estimated the initial reference CCF φ_{ref}^p for the p th component pair as,

$$258 \quad \varphi_{ref}^p(\tau) = \frac{1}{n} \sum_{t=1}^n \phi_t^p(\tau). \quad (15)$$

259 With the initial reference CCF, initial $\hat{\gamma}_t$ was measured using an extended Kalman filter/
 260 smoother described in the following subsections. Then we recalculated the reference
 261 as

$$262 \quad \varphi_{ref}^p(\tau) = \frac{1}{n} \sum_{t=1}^n \phi_t^p(\tau(1 + \hat{\gamma}_t)). \quad (16)$$

263 After recalculating $\hat{\gamma}_t$ with the revised reference, we measured the temporal variations
 264 that are discussed herein.

265 4.2 Extended Kalman filter

266 The state vector α_t was estimated by the recursive linear Kalman (forward) filter
 267 and (backward) smoother. The Kalman filter/smoother is a powerful solver of a state-
 268 space model, which obeys Gaussian distributions (e.g., Durbin & Koopman, 2012). The
 269 method has been applied for many geophysical problems (e.g., geodetic inversions, Segall
 270 & Matthews, 1997; Aoki et al., 1999), and recursive travel-time inversion in seismology
 271 (Ogiso et al., 2005). Since state vectors obey a normal distribution, the means and the
 272 covariance matrices characterized the statistics of the vector completely. Let us consider
 273 the conditional mean and covariance matrix of the state variables at time $t = 2 \cdots n$
 274 for given data through $\mathbf{Y}_1, \cdots, \mathbf{Y}_{t-1}$ as,

$$275 \quad \hat{\alpha}_{t|t-1} \equiv E(\alpha_t | \mathbf{Y}_1, \cdots, \mathbf{Y}_{t-1}) \quad (17)$$

$$276 \quad \hat{\mathbf{P}}_{t|t-1} \equiv Cov(\alpha_t | \mathbf{Y}_1, \cdots, \mathbf{Y}_{t-1}), \quad (18)$$

277 where n is number of the data, $E()$ represents expectation, and $Cov()$ represents covari-
 278 ance. $\hat{\alpha}_{t|t-1}$ is also known as the one-step ahead predictor (Durbin & Koopman, 2012).
 279 Since no data can constrain $\hat{\alpha}_{1|0}$ and $\hat{\mathbf{P}}_{1|0}$, they are given by the initial values: $\hat{\alpha}_{1|0} =$
 280 \mathbf{a}_1 and $\hat{\mathbf{P}}_{1|0} = \mathbf{P}_1$.

281 These are updated from the initial value \mathbf{a}_1 and \mathbf{P}_1 using the following equation:

$$282 \quad \hat{\alpha}_{t+1|t} = \hat{\alpha}_{t|t-1} + \mathbf{K}_t \mathbf{v}_t \quad (19)$$

$$283 \quad \hat{\mathbf{P}}_{t+1|t} = \hat{\mathbf{P}}_{t|t-1} - \mathbf{K}_t (\mathbf{Z}_t \hat{\mathbf{P}}_{t|t-1} \mathbf{Z}_t^T + \mathbf{H}_t) \mathbf{K}_t^T + \mathbf{Q}_t, \quad (20)$$

284 where Kalman gain \mathbf{K}_t is given by

$$285 \quad \mathbf{K}_t = \hat{\mathbf{P}}_{t|t-1} \mathbf{Z}_t^T (\mathbf{H}_t + \mathbf{Z}_t \hat{\mathbf{P}}_{t|t-1} \mathbf{Z}_t^T)^{-1}, \quad (21)$$

286 and the innovation vector \mathbf{v}_t is given by

$$287 \quad \mathbf{v}_t = \mathbf{Y}_t - \mathbf{M}_t(\hat{\alpha}_{t|t-1}). \quad (22)$$

288 Since the number of model parameters of 2 is much smaller than length of \mathbf{Y}_t of 36000
 289 (9 components \times 400 points), the matrix calculation of equation (21) can be reduced us-
 290 ing the following matrix inversion lemma (Tarantola & Valette, 1982; Ogiso et al., 2005),

$$291 \quad (\mathbf{H}_t + \mathbf{Z}_t \hat{\mathbf{P}}_{t|t-1} \mathbf{Z}_t^T)^{-1} = \mathbf{H}_t^{-1} - \mathbf{H}_t^{-1} \mathbf{Z}_t (\hat{\mathbf{P}}_{t|t-1}^{-1} + \mathbf{Z}_t^T \mathbf{H}_t^{-1} \mathbf{Z}_t)^{-1} \mathbf{Z}_t^T \mathbf{H}_t^{-1}. \quad (23)$$

292 Here we assumed that the errors of the CCF are independent of lag time, and the
 293 variances were the same throughout the lag time. Since we assumed that the covariance
 294 matrix of data error \mathbf{H}_t is represented by $\mathbf{H}_t = h_0 \mathbf{I}$ (equation (8)), the forward recur-
 295 sive equations (19) and (20) could be simplified as,

$$296 \quad \hat{\alpha}_{t+1|t} = \hat{\alpha}_{t|t-1} + \mathbf{\Xi}_t \Gamma_t \quad (24)$$

$$297 \quad \hat{\mathbf{P}}_{t+1|t} = \hat{\mathbf{P}}_{t|t-1} - \mathbf{\Xi}_t (\mathbf{S}_t \hat{\mathbf{P}}_{t|t-1} \mathbf{S}_t + h_0 \mathbf{S}_t) \mathbf{\Xi}_t^T + \mathbf{Q}_t, \quad (25)$$

298
 299
 300

where \mathbf{S}_t and $\mathbf{\Xi}_t$ are 2×2 matrices as:

$$\mathbf{S}_t \equiv \sum_p (\zeta_t^p)^T \zeta_t^p, \quad (26)$$

$$\mathbf{\Gamma}_t \equiv \sum_p (\zeta_t^p)^T \mathbf{v}_t^p, \quad (27)$$

$$\mathbf{\Xi}_t \equiv \left(\frac{1}{h_0} \hat{\mathbf{P}}_{t|t-1} - \frac{1}{h_0^2} \hat{\mathbf{P}}_{t|t-1} \mathbf{S}_t \left(\frac{\mathbf{S}_t}{h_0} + \hat{\mathbf{P}}_{t|t-1}^{-1} \right)^{-1} \right). \quad (28)$$

4.3 Kalman smoother

Next, let us consider the conditional mean $\hat{\alpha}_{t|n}$ and conditional covariance matrix $\hat{\mathbf{P}}_{t|n}$ of the state variables at time t for all data through $\mathbf{Y}_1, \dots, \mathbf{Y}_n$. With the $\hat{\alpha}_{t|t-1}$ and $\hat{\mathbf{P}}_{t|t-1}$ ($t = 2, \dots, n$) estimated in the previous subsection, they can be calculated by the following backward recursive equations,

$$\hat{\alpha}_{t|n} = \hat{\alpha}_{t|t-1} + \hat{\mathbf{A}}_t (\hat{\alpha}_{t+1|n} - \hat{\alpha}_{t|t-1}), \quad (29)$$

$$\hat{\mathbf{P}}_{t|n} = \hat{\mathbf{P}}_{t+1|t} - \mathbf{Q}_t + \hat{\mathbf{A}}_t (\hat{\mathbf{P}}_{t+1|n} - \hat{\mathbf{P}}_{t+1|t}) \hat{\mathbf{A}}_t^T. \quad (30)$$

where \mathbf{A}_t is defined by

$$\hat{\mathbf{A}}_t = \left(\mathbf{I} - \mathbf{Q}_t \hat{\mathbf{P}}_{t+1|t}^{-1} \right), \quad (31)$$

The recursive equations were applied successively backward as $t = n - 1, \dots, 1$.

4.4 Temporal change of seismic wave velocity

First, we tentatively estimated the temporal variations without the explanatory variables. For given hyper-parameters $r_t = e_t = 0$, $p_0 = 5 \times 10^{-4}$, $p_1 = 5 \times 10^{-5}$, we estimated the state variables using the extended Kalman filter/smoothen. Figure 4 shows the result of temporal variations in seismic velocity $\hat{\gamma}_{t|n}$ and the corresponding standard deviation by applying CCFs of the station pair between TKW and TKS. The figure shows clear seasonal variation, and the velocity drops coincide with strong rainfalls (blue bars in the figure). The red line shows the precipitation model (see the next section for details). This figure also shows a sudden velocity drop of about 0.1 % when the Kumamoto earthquake occurred in 2016. To detect signals associated with volcanic eruptions, we subtracted the precipitation effects and the earthquake drop from the temporal variations in seismic velocity. For the subtraction, we infer the hyper-parameters, which represent the model covariances, precipitation effects, and earthquake, drop by the Maximum Likelihood method in the next section.

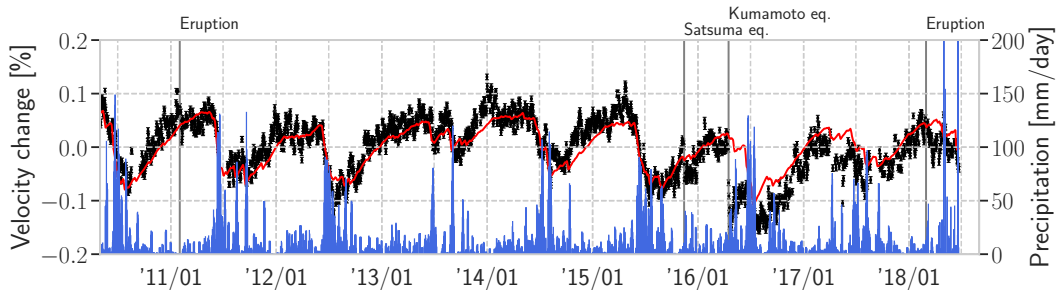


Figure 4. Row temporal changes of the pair between TKW and TKS with the prediction from the precipitation. The red line shows prediction by the precipitation model ($\tau_g = 195$ days, and $A_g = -6.84 \times 10^{-2}$ [%/m]), as described in the next section.

5 Maximum Likelihood Method for determining the hyper-parameters

In the previous section, we applied the extended Kalman filter/smoothen, assuming that the hyper-parameters were given at the lower level. This section shows how to infer the hyper-parameters using the Maximum Likelihood Method at the higher level of this technique.

The logarithmic likelihood $\ln L$ is given (e.g., Segall & Matthews, 1997; Durbin & Koopman, 2012) by

$$\ln L = -\frac{nN}{2} \ln 2\pi - \frac{1}{2} \sum_{t=1}^n \left(\ln(\det(\mathbf{F}_t)) + \hat{\mathbf{d}}_{t|t-1} \right), \quad (32)$$

where \mathbf{F}_t and $\hat{\mathbf{d}}_{t|t-1}$ are given by,

$$\mathbf{F}_t \equiv h_0 \mathbf{I} + \mathbf{Z}_t \hat{\mathbf{P}}_{t|t-1} \mathbf{Z}_t^T, \quad (33)$$

and

$$\hat{\mathbf{d}}_{t|t-1} = \frac{1}{h_0^2} \left(h_0 \mathbf{v}_t^T \mathbf{v}_t - \mathbf{\Gamma}_t^T \left(\hat{\mathbf{P}}_{t|t-1}^{-1} + \frac{\mathbf{S}_t}{h_0} \right)^{-1} \right) \mathbf{\Gamma}_t, \quad (34)$$

respectively (see Appendix A for details). We maximized the logarithmic likelihood $\ln L$ with respect to the hyper-parameters.

First, we describe how to model the hyper-parameters for explaining the precipitation effects and the reduction associated with the 2016 Kumamoto earthquake in the following two subsections.

5.1 A model for the precipitation effects

Many researchers have reported periodic changes in seismic wave velocity associated with external sources such as tides (e.g., Yamamura et al., 2003; Takano et al., 2014, 2019), thermoelastic effects (e.g., Hillers, Ben-Zion, et al., 2015; Wang et al., 2017), and snow loading (e.g., Wang et al., 2017). The correspondence between strong rainfall and the seismic velocity changes shown in Figure 4 suggests the dominance of the precipitation effect in this case. For modeling temporal changes of seismic wave velocity caused by precipitation, we considered two models: the model based on diffusion of a pore pressure (Talwani et al., 2007; Rivet et al., 2015; Lecocq et al., 2017; Wang et al., 2017), and the hydrological model (Sens-Schönfelder & Wegler, 2006).

The first model considered diffusion of pore pressure in a poroelastic medium with a spatial scale of several km, which induces seismic velocity changes. This model also required the sensitivity of seismic velocity to changes in pore pressure. As discussed in section 7.2, the sensitivity in this region is an order of magnitude smaller than the typical values. The diffusion of pore pressure also caused significant time delay, which is not consistent with the observations in this study.

The second model related the seismic velocity to the groundwater level at a shallow depth due to the precipitation (Sens-Schönfelder & Wegler, 2006). Since the groundwater level reaches a shallow depth of about 100 m in this region (Kagiyama et al., 1996; Tsukamoto et al., 2018), we regarded the second model more relevant. The response of the groundwater level to the precipitation is given by an exponential function (Sens-Schönfelder & Wegler, 2006; Kim & Lekic, 2019). The amount of groundwater storage g_t is given by

$$g_t = \int_t^\infty (p(\tau) - \langle p \rangle) e^{-\frac{t-(\tau+\delta)}{\tau_g}} d\tau, \quad (35)$$

where p is daily precipitation, δ shows delay time, τ_g is the parameter describing the decay, $\langle p \rangle$ is the average precipitation throughout the analyzed time period. We modeled

373 that the explanatory variable for precipitation r_t is proportional to g_t as,

$$374 \quad r_t = A_g g_t = A_g \int_t^\infty (p(\tau) - \langle p \rangle) e^{-\frac{t-(\tau+\delta)}{\tau_g}} d\tau, \quad (36)$$

375 where A_g is the sensitivity of seismic wave velocity to the amount of groundwater stor-
 376 age. Since there exists ambiguity of the modeling, A_g , τ_g , and δ should be constrained
 377 by the observations practically. We regard A_g , τ_g and δ as hyper-parameters, and infer
 378 their values by the Maximum Likelihood Method as shown later in this section.

379 To validate the second model quantitatively, we estimate the sensitivity A_g based
 380 on a physical model: density perturbation due to groundwater-level changes causes the
 381 temporal change associated with precipitation. Since surface waves are dominant in the
 382 wavefield in this frequency range, the depth sensitivity can be represented by that of the
 383 surface waves for a 1-D medium (Obermann et al., 2013). We consider only Rayleigh waves
 384 for simplicity, since a similar discussion can be applicable for Love waves. The phase ve-
 385 locity perturbation of Rayleigh waves δc can be related to perturbations of density ρ ,
 386 bulk modulus κ , and rigidity μ using the partial derivatives of phase velocity (Takeuchi
 387 & Saito, 1972) as,

$$388 \quad \frac{\delta c}{c} = \int \left(K_\rho(z) \frac{\delta \rho(z)}{\rho(z)} + K_\kappa(z) \frac{\delta \kappa(z)}{\kappa(z)} + K_\mu(z) \frac{\delta \mu(z)}{\mu(z)} \right) dz, \quad (37)$$

389 where c is the phase velocity, and K_ρ , K_κ and K_μ are the Fréchet derivatives relating
 390 the fractional perturbation of phase velocity $\delta c/c$ to the fractional perturbations $\delta \rho/\rho$,
 391 $\delta \kappa/\kappa$, $\delta \mu/\mu$. The Fréchet derivatives are also known as the depth sensitivity kernels. Fig-
 392 ure 5 shows an example of a depth sensitivity kernel at 0.6 Hz for the density and S-wave
 393 velocity models shown in the figure.

394 Working under the two assumption of (i) no temporal changes in bulk modulus κ
 395 and the rigidity μ , and (ii) the groundwater level of about 100 m, the temporal change
 396 r_t can be estimated as,

$$397 \quad r_t = \int K_\rho(z) \frac{\delta \rho(z)}{\rho(z)} dz \approx K_\rho(0) \frac{\rho_w g_t}{\rho(0)}, \quad (38)$$

398 where ρ_w is water density. Accordingly, A_g can be written by $K_\rho(0) \frac{\rho_w}{\rho(0)}$. For example,
 399 with the model shown by Figure 5, A_g is estimated to be -7.5×10^{-2} [%/m]. The con-
 400 sistency between this estimate of -7.5×10^{-2} [%/m] and the fitting result of $-6.84 \times$
 401 10^{-2} [%/m] supports our model. At higher frequencies (~ 5 Hz in this model), as the
 402 wavelength of the seismic surface wave is shorter than the groundwater level, the sen-
 403 sitivity significantly decreases.

404 For estimation of the hyper-parameters, initial values are required. We estimated
 405 them in two steps. First, using the initial reference CCF, $\hat{\gamma}_{t|n}$ was calculated for each
 406 station pair. In equation (5), \mathbf{R}_t is assumed to be $\mathbf{0}$. Then, A_g and τ_g were estimated
 407 by calculating the least squared difference between r_t and $\hat{\gamma}_{t|n}$. δ is fixed to 0. The red
 408 line in Figure 4 shows the initial estimate of a pair between TKW and TKS: $\tau_g = 195$ days
 409 and $A_g = -6.84 \times 10^{-2}$ [%/m]. This figure shows that the empirical model can pre-
 410 dict the seasonal variations well. To avoid the effects of the sudden drop due to the 2016
 411 Kumamoto earthquake, we used the data from before the earthquake in the estimation.

412 5.2 A model for the drops associated with 2016 Kumamoto earthquake

413 After the reduction of the effect of precipitation with the tentative hyper-parameters,
 414 the resultant temporal change shows sudden drops of seismic wave velocity associated
 415 with the 2016 Kumamoto earthquake (Figure 6). Since the drop related to the Kumamoto
 416 earthquake reaches 0.1 %, we modeled it by an exponential decay (Hobiger et al., 2016;
 417 Gassenmeier et al., 2016; Sens-Schönfelder & Eulenfeld, 2019) as,

$$418 \quad e_t = A_t e^{-\frac{t-t_0}{\tau_e}}, \quad (39)$$

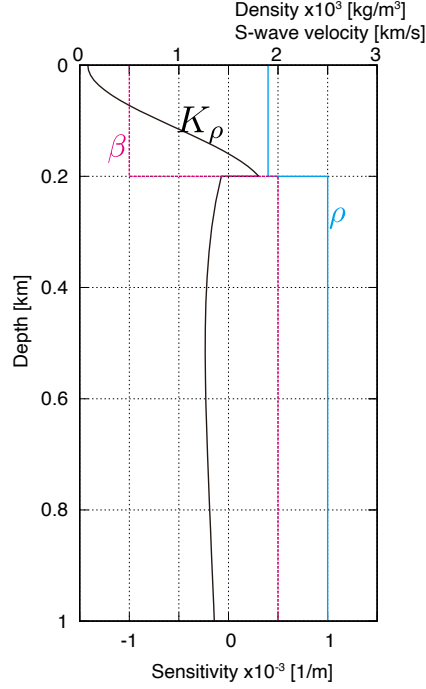


Figure 5. Depth sensitivity kernel to density perturbations at 0.6 Hz. The density ρ and the S-wave velocity β are plotted. P-wave velocities are 1.91 km/s from 0 to 0.2 km, and 4 km/s below 0.2 km.

419 where A_t is amplitude of the drop, t_0 is the origin time of the Kumamoto earthquake,
 420 and τ_e is the decay time. We omitted a term of non-recovering coseismic velocity drops
 421 (Hobiger et al., 2016) as the term could not be detected, as shown later (see Figure 10).

422 5.3 Estimation of the hyper-parameters by Maximum Likelihood Method

423 To reduce the number of hyper-parameters, we assumed that the expected value
 424 of the initial state variable \mathbf{a}_1 is given by $(1, \gamma_1)$, and the covariance matrix \mathbf{P}_1 is equal
 425 to \mathbf{Q}_t .

426 $\ln L$ is a function of hyper-parameters β , where

$$427 \quad \beta = (p_0, p_1, \tau_g, A_g, \delta, \gamma_1, A_e, \tau_e). \quad (40)$$

428 The logarithmic likelihood $\ln L$ was maximized with respect to the hyper-parameters us-
 429 ing a quasi-Newton method L-BFGS-B, which is a limited memory algorithm for solv-
 430 ing large nonlinear optimization problems subject to simple bounds on the variables (Zhu
 431 et al., 1994; Durbin & Koopman, 2012).

432 Figure 7 shows estimated hyper-parameters, which are well constrained by the ob-
 433 servations. Figure 7 (a) shows the model standard deviations of amplitude A_t of about
 434 $5 \times 10^{-3}\%$ and those of stretching factor γ_t of about 0.1%. We note that the observed
 435 data constrain the model standard deviations. Figure 7 (b) shows a trend of decreasing
 436 sensitivity A_g with decreasing decay time τ_g . This result suggests that the groundwater-
 437 level changes at shallower depths have shorter time decay τ_g , because the depth sensi-
 438 tivity kernel is negative and decreases to the ground surface (Figure 5). Figure 7 (c), which
 439 compares A_e and τ_e , shows the drop when the earthquake becomes larger, decreasing the

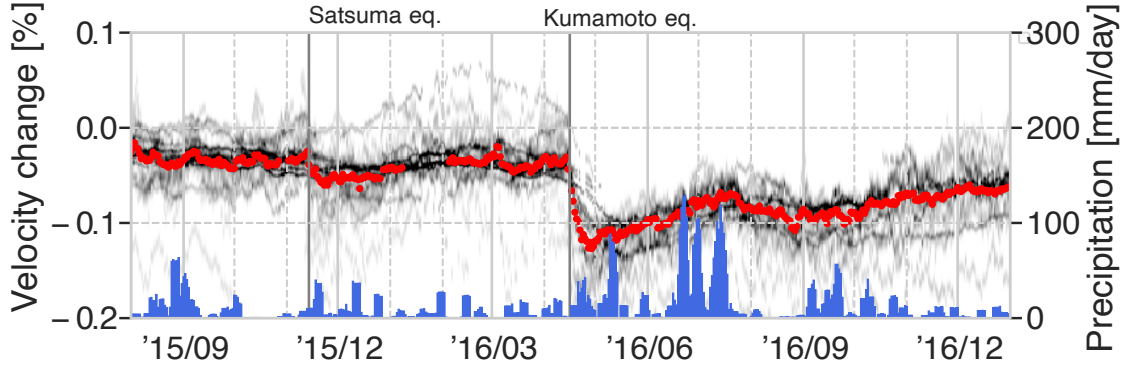


Figure 6. Velocity change associated with the 2016 Kumamoto earthquake. The seismic velocity drop when the earthquake occurred, and recovered over a time scale of three months. The grayscale shows marginal probability with all CCFs (see next section for details). The red dots show a median of all the measurements. The red dots also show a minor drop during the 2015 Satsuma earthquake.

440 recovery time. This result suggests that the stronger drop and shorter recovery occurred
 441 at shallower depths.

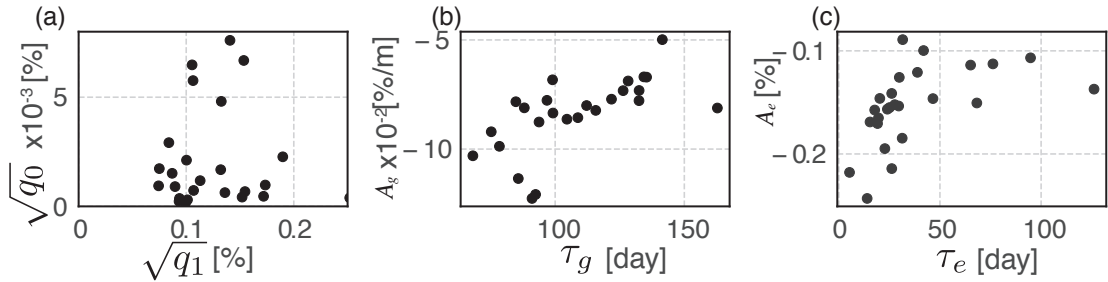


Figure 7. Estimated hyper-parameters. (a) scatter plot against standard deviations of the model: $\sqrt{q_0}$ and $\sqrt{q_1}$, (b) scatter plot against hyper-parameters of precipitation effects: τ_g and A_g , (c) scatter plot against hyper-parameters of the drop during the Kumamoto earthquake: A_e and τ_e .

442 To determine how well the observations constrain the hyper-parameters β , we esti-
 443 mated the sensitivity of the logarithmic likelihood of the perturbations around the opti-
 444 mal value β^{opt} . Figure 8 shows an increment of logarithmic likelihood to the optimal
 445 value of $\Delta \ln L$ as a function of a hyper-parameter. We perturbed each hyper-parameter
 446 within 50%, fixing all other hyper-parameters to the optimal values. Within this hyper-
 447 parameter range, the minima of $\Delta \ln L$ for all the hyper-parameters were smaller than
 448 -1.

449 Here we considered the appropriate number of hyper-parameters using the Akaike
 450 Information Criterion (AIC , Akaike, 1974) defined by

$$451 \quad AIC_K = -2 \ln \hat{L}_K + 2K, \quad (41)$$

452 where K is the number of hyper-parameters, and $\ln \hat{L}_K$ represents the maximum like-
 453 lihood for the K hyper-parameters. We choose the hyper-parameter if AIC_K decreases

454 with the addition of a new hyper-parameter: i.e. the increment $\Delta AIC \equiv AIC_K - AIC_{K-1}$
 455 is smaller than 0. Assuming that $\ln \hat{L}_{K-1} - \ln \hat{L}_K$ can be approximated by $\Delta \ln L$ shown
 456 in Figure 8, the ΔAIC is written by $2(\Delta \ln L + 1)$. The addition of a hyper-parameter
 457 is appropriate if $\Delta \ln L < -1$. Assuming that the ambiguity of each parameter is about
 458 50%, for example, β_i is fixed at $0.5\beta_i^{opt}$ as the prior value. Since all the $\Delta \ln L$ at $\beta_i/\beta_i^{opt} =$
 459 0.5 in Figure 8 are smaller than -1 , all the hyper-parameters used meet this condition.
 460 This choice of hyper-parameters also makes the iterations of the L-BFGS-B method stable.
 461

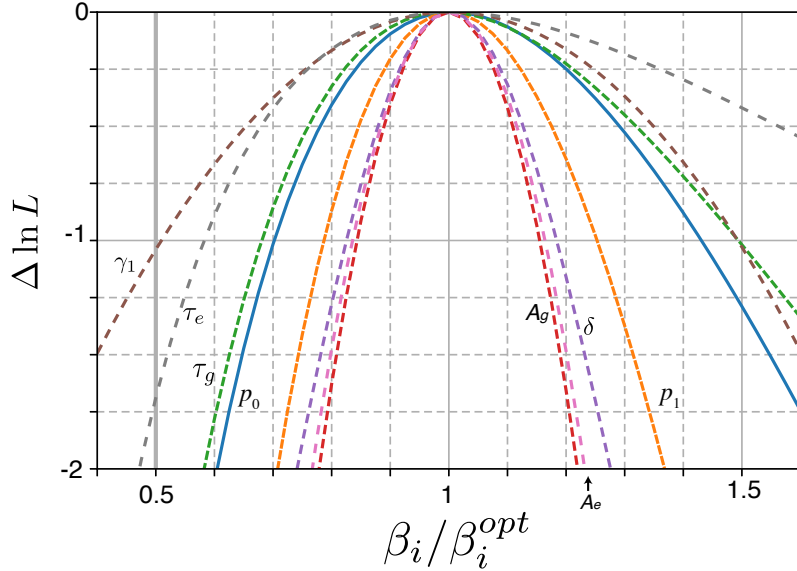


Figure 8. Logarithmic likelihood as a function of the normalized hyper-parameters. The horizontal axis shows relative value of hyper-parameters, and the vertical axis shows increments of logarithmic likelihood to the optimal value $\ln L(\beta^{opt})$. The corresponding hyper-parameters (β_i) are also shown in this figure.

462 6 Temporal changes of seismic wave velocity

463 Using the inferred hyper-parameters, we estimated state variables for all pairs of
 464 stations. Red lines in the upper triangular portion of Figure 9 show the total temporal
 465 changes of seismic wave velocity $\hat{\gamma}_{t|n} + r_t + e_t$. The blue lines show only the explanatory
 466 variables $r_t + e_t$ for precipitation and the earthquake. The explanatory variables
 467 can explain majority of the aspects of the estimated temporal changes.

468 The lower triangular portion of Figure 9 shows the resultant $\hat{\alpha}_{t|n}$. The blue lines
 469 show the amplitude $\hat{A}_{t|n}$, which show the local minimum in 2015. High activities of low-
 470 frequency volcanic tremor at Mt. Aso (Figure 1) could distort the coherency (Kaneshima
 471 et al., 1996; Hendriyana & Tsuji, 2019; Sandanbata et al., 2015). The red lines show seismic
 472 velocity changes, $\hat{\gamma}_{t|n}$, after the subtraction of the explanatory variables. They show
 473 a consistent long term variation with a time scale of about five years with an amplitude
 474 of about 0.05 %. Although most station pairs do not show significant temporal changes
 475 associated with the 2011 eruption, the pair between SMW and SMN shows a significant
 476 drop in 2011. The upper triangular portion shows the precipitation effect and the drop
 477 associated with the earthquake are well subtracted using the explanatory variables.

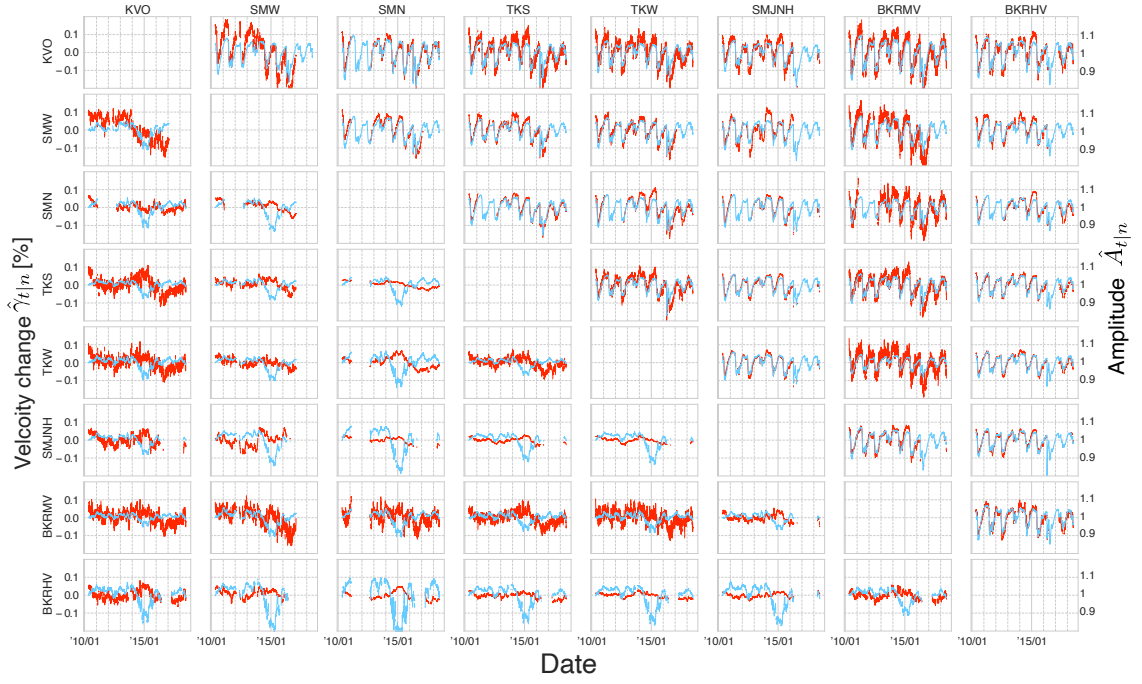


Figure 9. The lower triangular portion: resultant $\hat{\alpha}_{t|n}$. The red lines show seismic velocity change $\hat{\gamma}_{t|n}$ within 0.1%. The blue lines show the amplitude perturbations $\hat{A}_{t|n}$, which show a local minimum in 2015. The upper triangular portion: Blue lines show estimated seismic velocity changes $r_t + e_t$, which explain the precipitation effect and the drop during the Kumamoto earthquake, whereas red ones show estimated whole seismic velocity changes $\hat{\gamma}_{t|n} + r_t + e_t$.

478 To discuss the long-term variations, we considered the marginal probability den-
 479 sity with all pairs of stations. Figure 10(a) shows the marginal probability density over
 480 8 years with an assumption that each measurement is independent. The probability den-
 481 sity $f_t(\gamma)$ as a function of seismic velocity change γ is defined by

$$482 \quad f_t(\gamma) \equiv \frac{1}{28} \sum_{j=1}^{28} \mathcal{N}(^j\hat{\gamma}_{t|n}, ^j\hat{q}_{t|n}), \quad (42)$$

483 where \mathcal{N} represents normal distribution, $^j\hat{\gamma}_{t|n}$ is the conditional mean of seismic veloc-
 484 ity changes, $^j\hat{q}_{t|n}$ is the corresponding conditional covariance, j indicates a station pair,
 485 and 28 is the total number of station pairs. The marginal probability density (Figure
 486 10(a)) shows no significant changes associated with the 2011 and 2018 eruptions of Shinmoe-
 487 dake. However, areal strain calculated from GNSS observation shows inflation and de-
 488 flation due to changes in the magma reservoir during the 2011 eruption, and the 2018
 489 eruption (Nakao et al., 2013; Kozono et al., 2013; Yamada et al., 2019) (Figure 10(b)).
 490 The areal strain also shows the static change due to the 2016 Kumamoto earthquake,
 491 whereas $f_t(\gamma)$ does not show significant static change.

492 Apart from jumps of the areal strain associated with the eruptions and the earth-
 493 quake, both the seismic velocity changes and the areal strain (Figure 10) show tempo-
 494 ral variations with a time scale of about one year with local maxima in January 2012 and
 495 January 2013. After 2014, such temporal variations are no longer observed for both. One
 496 possible origin of the variations is the long term variations in groundwater levels (e.g.,
 497 Lecocq et al., 2017). When modeling groundwater level in equation (35), we assumed
 498 constant drainage. Nevertheless, under realistic conditions, the drainage may change with
 499 time. Since the areal strain also shows a similar undulation pattern from 2010 to 2013,
 500 such a long-term variation may cause large scale deformations. The induced pore pres-
 501 sure change (Talwani et al., 2007) at deeper depth, on the order of km, could also cause
 502 seismic velocity changes (Wang et al., 2017; Rivet et al., 2015). In this study, however,
 503 the hydrological data were insufficient to verify this hypothesis.

504 7 Discussions

505 In the following subsections, we discuss two specific events: the drop of seismic wave
 506 velocity associated with the Kumamoto earthquake and the 2011 Shinmoe-dake erup-
 507 tion. Based on the observed features, we discuss the magma pathway beneath Shinmoe-
 508 dake.

509 7.1 The drop of seismic wave velocity after the Kumamoto earthquake

510 Our results show a sudden drop during the Kumamoto earthquake followed by a
 511 recovery from 10 to 100 days (Figure 7). Since the probability density $f_t(\gamma)$ does not show
 512 non-recovering coseismic velocity drops due to the static areal-strain change (Figure 10),
 513 the observed static strain change could not be the dominant source. Near-surface dam-
 514 age beyond the linear elastic regime could be a possible origin. For the discussion, we
 515 compare the susceptibility, which is defined by the ratio between observed reductions in
 516 seismic velocity and the estimated dynamic stress with that of the 2011 Tohoku earth-
 517 quake (Brenugier et al., 2014).

518 We estimated the dynamic stress from the observed peak ground velocity (PGV)
 519 (Gomberg & Agnew, 1996). PGV in this region was about 5 cm/s during the Kumamoto
 520 earthquake, which was averaged over 3 components of PGV measured by the K-net, strong-
 521 motion seismograph network. The dynamic stress $\Delta\sigma \approx \mu v/c$ was estimated to be 0.5 MPa,
 522 where μ is the mean crustal shear modulus (~ 30 GPa), v is PGV, and c is the mean
 523 wave phase velocity of the Rayleigh wave (~ 3 km/s) (Brenugier et al., 2014). The sus-
 524 ceptibility (Brenugier et al., 2014), which is defined by the ratio between observed re-

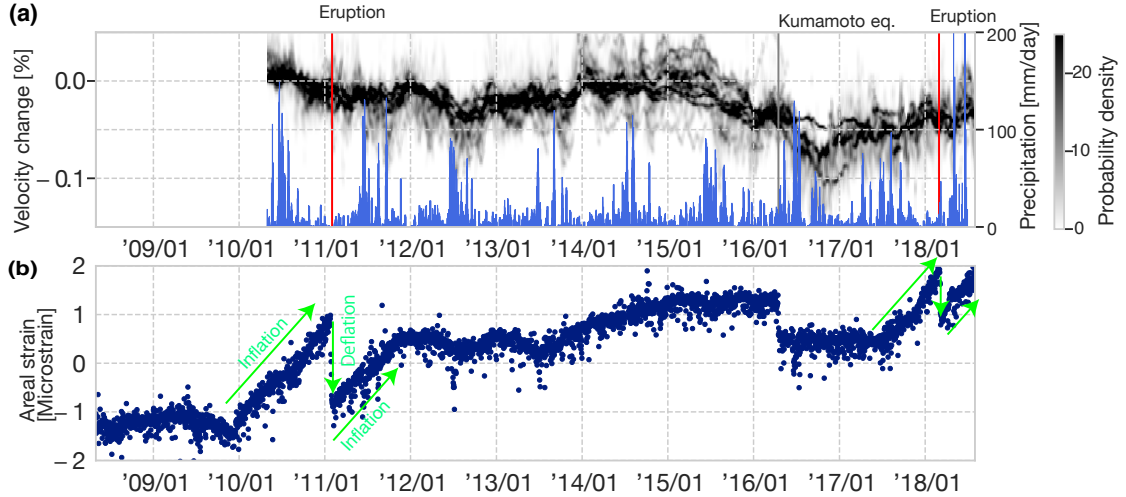


Figure 10. (a) Marginal probability density of all pairs of stations. The blue bars show daily precipitation data at the JMA meteorological station. The estimated seismic velocities scatter from Oct. 2014 to May 2015 when the activity of low frequency tremor at Mt. Aso occurs. (b) Areal strain calculated from three GEONET stations: Ebino, Miyakonojou2 and Makizono shown in Figure 1.

525 reductions in seismic velocity $\Delta c/c$ ($\sim 2 \times 10^{-3}$) and the estimated dynamic stress 0.5 MPa,
 526 was about $4 \times 10^{-3} \text{ MPa}^{-1}$. This value is larger than susceptibility in the Mt. Fuji area
 527 and along the Tohoku volcanic during the Tohoku earthquake, whose value is about $1.5 \times$
 528 10^{-3} MPa^{-1} (Brenquier et al., 2014). This observation suggests that the pressurized ge-
 529 offluid in the upper crust and/or near-surface is a possible origin for the seismic veloci-
 530 ty changes.

531 We discuss the mechanism of the observed seismic velocity change as caused by the
 532 pressurized fluid. The exponential decay time scales ranged from 10 to 100 days, sug-
 533 gesting the lack of a relaxation process longer than 100 days (Snieder et al., 2017). The
 534 estimation of relatively short time scales dismisses the mechanisms of post-seismic re-
 535 laxation of stress (e.g., Brenquier, Shapiro, et al., 2008) and diffusion of geofluid in the
 536 crust (Wang et al., 2019). The absence of non-recovering coseismic velocity drop dur-
 537 ing the 2016 Kumamoto earthquake suggests that the pressurization of geofluid in the
 538 linear elastic regime is unlikely to be the origin. This hypothesis is also consistent with
 539 the observation that the 2011 Tohoku earthquake did not trigger any volcanic and seis-
 540 mic activities in this region (Miyazawa, 2011). Near-surface damage due to the strong
 541 ground motions beyond the linear elastic regime, where rich groundwater exists, could
 542 be a plausible origin.

543 7.2 Temporal changes during the volcanic eruptions in 2011

544 The probability density of all the station pairs f_t (Figure 10(a)) does not show any
 545 temporal change associated with the volcanic eruptions from January 2011 to February
 546 2011. However, geodetic observation showed the gradual magma intrusion over the time
 547 scale of a year and the discharge during the eruption (see the areal strain in Figure 10(b)).
 548 The geodetic source was located 5 km to the northwest of the summit at a depth of about
 549 8 km (Nakao et al., 2013). Although the volumetric change caused enough strain (about

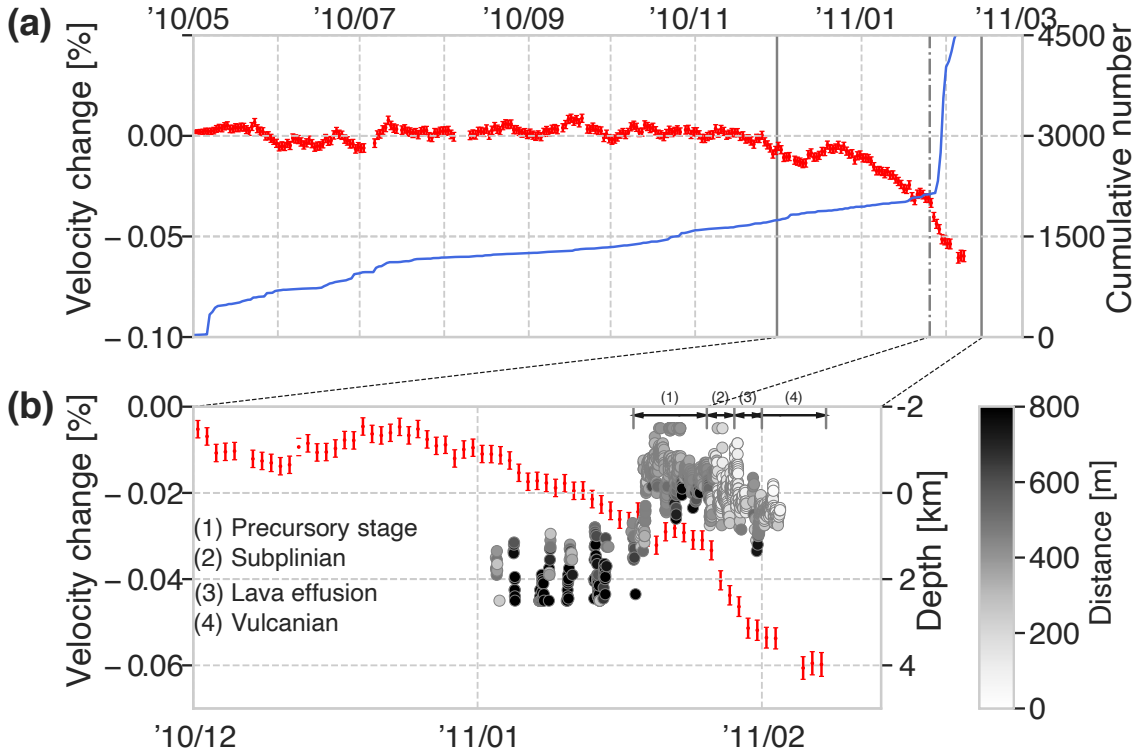


Figure 11. (a) Seismic velocity changes $\hat{\gamma}_{t_n}$ for the pair between SMN and SMW shown by red bars. The station SMN was damaged during the eruption. The line in sky blue shows the cumulative number of volcanic earthquakes determined by JMA below Shinmoe-dake. (b) Enlarged figure from October 1st, 2010 to February 14th, 2011. The panel also shows the depth of volcanic tremor (Ichihara & Matsumoto, 2017). The color of a circle shows the horizontal distance from the center of the summit to the hypocenter. Four periods: (1) Precursory stage, (2) Sub-Plinian, (3) Lava effusion, and (4) Vulcanian (e.g., Nakada et al., 2013; Kozono et al., 2013) are also shown.

550 1.5 microstrains estimated from GNSS as shown by Figure 10) to cause the seismic velocity change with a typical sensitivity of seismic velocity change in a linear elastic regime
 551 (e.g., Takano et al., 2017), as discussed later, our results do not show a significant change.
 552 These observations could provide a clue for inferring the state of the material in the upper
 553 crust.
 554

555 Despite of the absence of observed temporal changes for most station pairs during
 556 the 2011 eruption (Figure 9), one station pair close to the crater (SMW and SMN)
 557 showed a significant drop of seismic velocity (red lines in Figure 11). Figure 11 shows
 558 the resultant temporal variations between the station pair (SMW and SMN) from May
 559 2010 to May 2011. The gradual drop of seismic velocity that preceded the eruption by
 560 one month. Since the station SMN was broken 10 days after the main phase of the 2011
 561 eruption, the post-eruption recovery cannot be discussed.

We discuss the 2011 Shimoedake-eruption based on the two observed temporal variations in seismic wave velocity: (i) no observed temporal variations with the one-year inflation of the magma reservoir, (ii) only the station pair close to the crater detected the gradual decrease preceding the eruption by one month.

First, we consider why the observation only shows temporal variation at one pair. Figure 12 shows areal strain, induced by the point volumetric source, by deflation caused by the migration of magma to the surface. The volumetric source modeled by Nakao et al. (2013) was located at a point (longitude 130.831°E, latitude 31.942°N, depth 8.35 km), which is about 6.9 km northwestern to Shinmoe-dake. The modeled volume change of the deflation is $13.35 \times 10^6 \text{ m}^3$. This model can explain the GNSS observations during the deflation in 2011: i.e., this model can explain the observed drop of areal strain based on GNSS shown by Figure 10(b).

The typical areal strain at a depth of 3 km above the volumetric source is 5×10^{-6} , and the typical value of the bulk modulus at a depth of 3 km is 30 GPa. Since the corresponding stress change is $1.5 \times 10^5 \text{ Pa}$, the stress sensitivity of seismic velocity change is estimated to be less than $6 \times 10^{-10} \text{ Pa}^{-1}$. As this estimated stress sensitivity is an order of magnitude smaller than the past studies at this depth (Takano et al., 2017), our results suggest that the crustal material has lower sensitivity to static stress changes in a linear elastic regime than other regions. This observation is also consistent with that the 2016 Kumamoto earthquake caused only recovering coseismic velocity drops due to dynamic stress but no permanent ones in response to static changes in areal strain (Figure 10). The observed lack of sensitivity is also consistent with our model of precipitation effects, which does not require stress sensitivity of the seismic velocity.

One possible interpretation of the observed low sensitivity or lack of sensitivity could be related to the aspect ratio of crack and/or fluid inclusion of the medium. The low sensitivity suggests that the shape of cracks could be circular (Shapiro, 2003). The P-wave velocity at 3 km is about 5.5 km/s (Tomatsu et al., 2001), and the S-wave velocity is approximately 3.1 km/s (Nagaoka, 2020), suggesting that fraction of the geofluid and crack density should be small. The inclusions of the geofluid could also be isolated because the 3-D inversion of the anomalous magnetotelluric data in this region showed a highly resistive body above the volumetric source (Aizawa et al., 2014).

Next, we considered the spatial localization of the gradual decrease near the crater precedes the eruption by one month. For simplicity, we considered the homogeneous medium with seismic velocity c of 2 km/s, which correspond to a typical group velocity of Rayleigh waves. We evaluated the sensitivity kernel of the travel time from a point \mathbf{s}_1 to a point \mathbf{s}_2 for local changes of seismic velocities as

$$\left. \frac{\delta c(t)}{c} \right|_{app} = \frac{1}{ct} \int_S K(\mathbf{s}_1, \mathbf{s}_2, \mathbf{r}, t) \delta v(\mathbf{r}) dS(\mathbf{r}), \quad (43)$$

where $\left. \frac{\delta c(t)}{c} \right|_{app}$ is the apparent velocity change, which corresponds to the measurement, t is travel time, $\delta v(\mathbf{r})$ is the perturbation of the seismic velocity at a point \mathbf{r} , S represents the whole surface area, and K is a sensitivity kernel (Pacheco & Snieder, 2005) given by,

$$K(\mathbf{s}_1, \mathbf{s}_2, \mathbf{r}, t) = \frac{\int_0^t p(\mathbf{s}_1, \mathbf{r}, t') p(\mathbf{r}, \mathbf{s}_2, t - t') dt'}{p(\mathbf{s}_1, \mathbf{s}_2, t)}, \quad (44)$$

where $p(\mathbf{s}_1, \mathbf{s}_2, t)$ is the probability density that the wave traveled from \mathbf{s}_1 to \mathbf{s}_2 during time t (Machacca et al., 2019): i.e. $p(\mathbf{s}_1, \mathbf{r}, t)$ satisfies the normalization condition given by,

$$\int_S p(\mathbf{s}_1, \mathbf{r}, t) dS(\mathbf{r}) = 1. \quad (45)$$

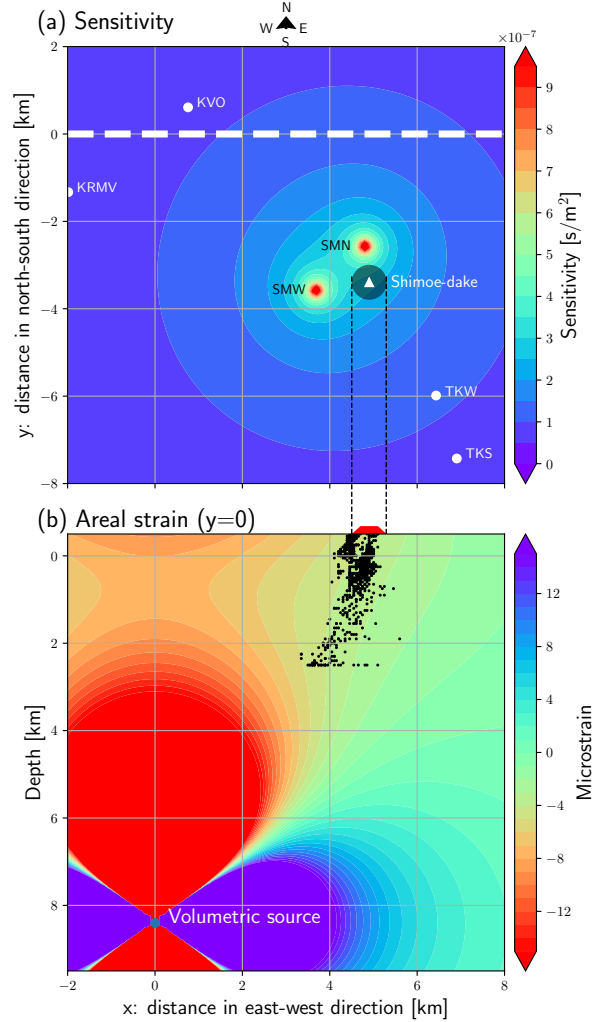


Figure 12. (a) Sensitivity kernel (Pacheco & Snieder, 2005; Obermann et al., 2013) at lapse time of 60 s. The scattering mean free path is assumed to be 5000 m. (b): Areal strain induced by the point volumetric source ($y = 0$). The model (Nakao et al., 2013) is based on geodetic observation. This panel also shows hypocenters of volcanic tremors given by Ichihara and Matsumoto (2017). Although the hypocenters below 1 km were shifted in a westward direction, the shift might be caused by limited station coverage. We calculated the strain caused by the volumetric source using an inflation point source model (Okada, 1992) in a 3D elastic half-space with a rigidity of 10 GPa, and Poisson’s ratio of 0.25. For simplicity, we assumed that the height of the surface in this area is fixed to 0.5 km above sea level.

608 Here p is given in the analytic form of the radiative transfer for isotropic scattering in
 609 2-D (Obermann et al., 2013) as,

$$610 \quad p(r, t) = \frac{\exp\left(-\frac{ct}{l}\right)}{2\pi r} \delta(ct-r) + \frac{1}{2\pi lct} \left(1 - \frac{r^2}{c^2 t^2}\right)^{-1/2} \exp\left(\frac{\sqrt{c^2 t^2 - r^2} - ct}{l}\right) H(ct-r), \quad (46)$$

611 where l is the scattering mean free path of 5000 m, r is the distance between \mathbf{s}_1 and \mathbf{s}_2 ,
 612 and H is the Heaviside step function. The scattering mean free path is longer than the
 613 typical value (about 1 km at 1–10 Hz) at active volcanoes (e.g., Yamamoto & Sato, 2010;
 614 Chaput et al., 2015). Because the longer wavelength at the dominant frequency of about
 615 0.3 Hz tends to homogenize the effects of lateral heterogeneities, the scattering mean free
 616 path could be longer. Moreover, the area of our interest includes both volcanic and non-
 617 volcanic areas. Although mean free paths in the volcanic edifice should be shorter in the
 618 nonvolcanic areas, the average could be longer. Figure 12 (a) shows the sensitivity ker-
 619 nel at the lapse time $t = 60$ s, which shows two local maxima at the stations. If the dam-
 620 aged area is 1 km at the Shinmoe-dake, which is about twice as the crater size, the ve-
 621 locity drop within the area is estimated to be about 5%. A trade-off exists between δc
 622 and the damaged area.

623 We considered three possible origins of the localized seismic velocity changes: (i)
 624 stress sensitivity of the edifice in a linear elastic regime, (ii) density perturbation due to
 625 the magma intrusion, and (iii) damage accumulation near the crater. We already showed
 626 that the stress sensitivity in this region is small, though past studies (e.g., Sens-Schönfelder
 627 et al., 2014) have shown that stress changes due to the increased pressure of the magma
 628 reservoir could cause the observable seismic velocity change. Moreover, no other infla-
 629 tion/deflation sources were observed before the 2011 Shinmoe-dake eruption. Next, we
 630 considered density perturbation, as in the case of the precipitation effect. Kozono et al.
 631 (2013) estimated the erupted volume based on geodetic and satellite observations. The
 632 total extruded volume of dense rock equivalence was estimated to about 3×10^7 m³, and
 633 the density was 2500 kg/m³. In order to constrain the upper limit of seismic velocity re-
 634 duction due the density perturbation, we assumed that the magma was stored at a depth
 635 shallower than 0.6 km where Rayleigh waves have the greater sensitivity (Figure 5). The
 636 equation (38) leads to the upper limit of about 0.6% drop in seismic velocity, which is
 637 significantly smaller than our observations (5%). Therefore we conclude that the observed
 638 seismic velocity drop with a time scale of about one month near the crater could be caused
 639 by cumulative damage beyond the linear elastic regime, induced by the pressure exerted
 640 by the magma reservoir on the edifice (Olivier et al., 2019).

641 The location of the volcanic tremor (TR) source also gives us a clue as to the magma
 642 or gas movement before the main eruption. Ichihara and Matsumoto (2017) located TR
 643 sources from seven stations recording continuous volcanic tremor before and during the
 644 sub-Plinian eruptions using the amplitude distribution. Figure 11(b) shows the source
 645 depth of TR from January 3rd, 2011, to February 2nd, 2011. Prior to January 2011, the
 646 TR amplitudes were too small to locate. Before the precursory stage of the eruption, the
 647 source depths were approximately 2 km. With increased damage, the source depth mi-
 648 grated upward to around sea level when the precursory stage was initiated. When the
 649 sub-Plinian eruption started, the decreasing rate of seismic velocity changes became steeper.
 650 This observation suggests that the magma migration from 2 km to the surface increased
 651 the damage of the sub-surface material. Figure 12(b) shows the depth section of the source
 652 locations. They also support the vertical magma migration beneath the summit. The
 653 sources below 1 km could be biased in the western direction, due to the limited station
 654 distribution.

655 Ambient noise tomography in this region (Nagaoka, 2020) revealed the magma reser-
 656 voir imaged as a low S-wave velocity body with a strong radial anisotropy of up to 30%.
 657 It was located just below the geodetic source, and the horizontal scale was about 15 km
 658 (Figure 13). Horizontally multilayered sills can explain the strong radial anisotropy with

659 and without partial melts. The connection between the sills can enable the horizontal
 660 magma migration from the magma reservoir to Shinmoe-dake. The geochemical anal-
 661 ysis (Nakada et al., 2013; Suzuki et al., 2013) showed the basaltic magma was stored at
 662 the magma reservoir. The viscosity is low enough to develop the sill complex, and the
 663 mobility is high during the eruption. In January 2011, due to damage, the pressuriza-
 664 tion of the magma began to decrease the seismic velocity gradually. The pressurization
 665 also activated TR activity at depth of 2 km (Figure 13(a)). During this stage, the sili-
 666 cic magma was mixed with the basaltic magma (Suzuki et al., 2013). Since the viscos-
 667 ity of the silicic magma is estimated to be high (about 1.2×10^6 Pa·s, Suzuki et al., 2013),
 668 the magma fluid could be isolated.

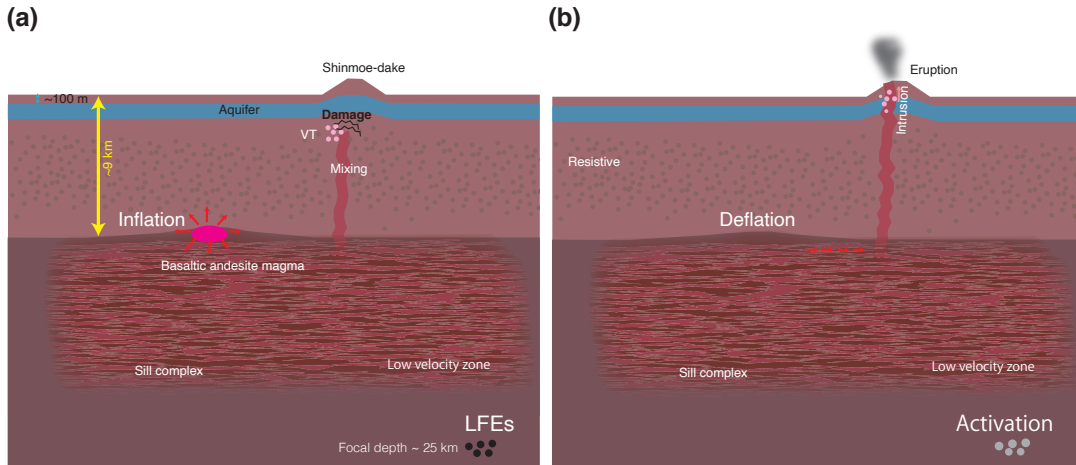


Figure 13. Schematic of the 2011 eruption: (a) from one month before until just before the eruption, and (b) during the eruption. LFEs represent low frequency earthquakes (Kurihara et al., 2019), and TR represents volcanic tremor (Ichihara & Matsumoto, 2017).

669 8 Conclusions

670 In this study, seismic interferometry was applied to a seismic network around Shinmoe-
 671 dake to monitor the seismic velocity change for eight years from May 2010 to April 2018.
 672 We applied the stretching method (Sens-Schönfelder & Wegler, 2006) for a cross-correlation
 673 function calculated for each pair of stations using continuous ambient noise data. To sep-
 674 arate the variations of volcanic origin from environmental variations, we developed a new
 675 technique based on a state-space model: the parameters (e.g., seismic velocity change)
 676 were estimated by an extended Kalman filter, and the hyper-parameters (the seismic re-
 677 sponse to the precipitation, the response to the Kumamoto earthquake, and covariances
 678 of the parameters) were estimated by the Maximum Likelihood Method. The resultant
 679 seismic velocity changes show clear seasonal variation originating from precipitation as
 680 well as a drop associated with the 2016 Kumamoto earthquake.

681 After the effects of precipitation and the earthquake were subtracted, most of the
 682 seismic velocity changes did not show any changes associated with the eruptions. Since
 683 the strain changes caused by the volumetric change during the 2011 eruption (Nakao et
 684 al., 2013) were about five microstrains at depths from 0 to 2 km above the source, the
 685 stress sensitivity of the seismic velocity in a linear elastic regime was significantly smaller
 686 than other areas (e.g., Takano et al., 2017). The observed lack of sensitivity suggests the

687 smaller aspect ratio of crack and less fluid inclusion in the upper crust (Shapiro, 2003),
 688 which is consistent with the highly resistive body above the volumetric source (Aizawa
 689 et al., 2014). The P-wave velocity at 3 km is about 5.5 km/s (Tomatsu et al., 2001), and
 690 the S-wave velocity is about 3.1 km/s (Nagaoka, 2020), indicating small melt fraction
 691 and crack density.

692 Only one station pair located in the neighborhood of the crater showed a gradual
 693 decrease in seismic velocity, which preceded the eruption by one month. The maximum
 694 drop of the seismic velocity was about 0.05% during the 2011 eruption. The sensitivity
 695 kernel (Pacheco & Snieder, 2005) of this observation suggests that the seismic wave drop
 696 of about 5% was localized at the crater with a spatial dimension of about one km². In
 697 this region, P wave travel time tomography revealed a pipe-like structure of high-velocity
 698 under the summit craters from 1.5 to 0.5 km below sea level (Tomatsu et al., 2001). The
 699 fluid intrusion started to damage the high-velocity pipe structure one month before the
 700 eruption. Until January 16th 2011, the source depths of TR were around 2 km (Ichihara
 701 & Matsumoto, 2017) although the TR amplitudes were too small to locate before Jan-
 702 uary 2011. With increasing damage, the source depth migrated upward to around sea
 703 level when the precursory stage started on January 16th. Then, the magma migrated
 704 from the depth of 2 km to the surface. The magma migrated vertically from the reser-
 705 voir imaged as a low S-wave velocity body just below the geodetic source.

706 Notation

707 **t** : Days from 1 May 2010 (JST) = $1, \dots, n$
 708 **p** : A component pair (9 components: $R - R, R - T, \dots, Z - Z$).
 709 **τ** : Lag time of a CCF
 710 **$\phi_t^p(\tau)$** : Observed CCF
 711 **y_t^p** : The data vector consisting of $\phi_t^p, \tau = (-\tau_e, -\tau_e + 1 \dots - \tau_s, \tau_s \tau_s + 1 \dots \tau_e)$
 712 **$\alpha_t \equiv (A_t, \gamma_t)^T$** : The state variable α_t with the amplitude A_t and stretching factor γ_t
 713 **$R_t \equiv (0, r_t)^T$** : Explanatory variables related to precipitation, where r_t explains the stretch-
 714 ing factor
 715 **$E_t \equiv (0, e_t)^T$** : Explanatory variables associated with the 2016 Kumamoto earthquake,
 716 where e_t explains the stretching factor
 717 **$m^p(A_t, \gamma_t; \tau)$** : a model of an observed CCF
 718 **$\varphi_{ref}^p(\tau)$** : The reference CCF
 719 **$H_t \equiv h_0 I$** : A prior data covariance matrix, where h_0 is a prior data covariance
 720 **I** : Identity matrix
 721 **Q_t** : A prior model covariance matrix
 722 **$a_1 \equiv (A_1, \gamma_1)^T$** : A prior initial value of the state variable
 723 **P_1** : A prior model covariance matrix of the initial value

724 Acknowledgments

725 I am grateful to people for maintaining the networks and making the data readily avail-
 726 able. This work was supported by JSPS KAKENHI Grant Number JP17H02950 and JP17K05625.
 727 This research made use of ObsPy (Krischer et al., 2015), NumPy (Van Der Walt et al.,
 728 2011) and SciPy (Virtanen et al., 2020). Figure 1 was prepared with GMT programs (Wessel
 729 et al., 2013). We thank M. Takeo, Y. Takei and T. Ohminato for the valuable discus-
 730 sions. We also thank Nori Nakata, Julien Chaput and Rick Aster for their helpful and
 731 constructive feedback that has improved this manuscript.

732 **Data and materials availability:**

733 We used data from F-net (doi.org/10.17598/nied.0005), Hi-net (doi.org/10.17598/nied.0003), V-net (doi.org/10.17598/nied.0006) and K-net (doi.org/10.17598/nied.0004), which are managed by the National Research Institute for Earth
734 Science and Disaster Prevention (NIED), Japan. In situ precipitation observations were
735 obtained from the Automated Meteorological Data Acquisition System (AMeDAS) of
736 the Japan Meteorological Agency (JMA) are available at <http://www.data.jma.go.jp/obd/stats/etrn/index.php> (in Japanese). F3 solutions of GNSS data are provided by
737 Geospatial Information Authority of Japan (<http://www.gsi.go.jp>). Daily CCFs in
738 this study are available at the Zenodo web page (<https://doi.org/10.5281/zenodo.2539824>). The python code is also available at the Zenodo web page (<https://doi.org/10.5281/zenodo.3969122>).
739
740
741
742
743

744 References

- 745 Aizawa, K., Koyama, T., Hase, H., Uyeshima, M., Kanda, W., Utsugi, M., ...
746 Ogawa, Y. (2014). Three-dimensional resistivity structure and magma plumbing
747 system of the Kirishima Volcanoes as inferred from broadband magnetotelluric
748 data. *Journal of Geophysical Research: Solid Earth*, *119*(1), 198–215. doi:
749 10.1002/2013JB010682
- 750 Akaike, H. (1974). A New Look at the Statistical Model Identification. *IEEE*
751 *Transactions on Automatic Control*, *19*(6), 716–723. doi: 10.1109/TAC.1974
752 .1100705
- 753 Aoki, Y., Segall, P., Kato, T., Cervelli, P., & Shimada, S. (1999). Imaging magma
754 transport during the 1997 seismic swarm off the Izu Peninsula, Japan. *Science*,
755 *286*(5441), 927–930. doi: 10.1126/science.286.5441.927
- 756 Bensen, G. D., Ritzwoller, M. H., Barmin, M. P., Levshin, A. L., Lin, F., Moschetti,
757 M. P., ... Yang, Y. (2007). Processing seismic ambient noise data to obtain re-
758 liable broad-band surface wave dispersion measurements. *Geophysical Journal*
759 *International*, *169*(3), 1239–1260. doi: 10.1111/j.1365-246X.2007.03374.x
- 760 Brenguier, F., Campillo, M., Hadziioannou, C., Shapiro, N., Nadeau, R. M., &
761 Larose, E. (2008). Postseismic relaxation along the san andreas fault at
762 parkfield from continuous seismological observations. *Science*, *321*(5895),
763 1478–1481.
- 764 Brenguier, F., Campillo, M., Takeda, T., Aoki, Y., Shapiro, N. M., Briand, X.,
765 ... Miyake, H. (2014). Mapping pressurized volcanic fluids from in-
766 duced crustal seismic velocity drops. *Science*, *345*(6192), 80–82. doi:
767 10.1126/science.1254073
- 768 Brenguier, F., Rivet, D., Obermann, A., Nakata, N., Bouoé, P., Lecocq, T., ...
769 Shapiro, N. (2016). 4-D noise-based seismology at volcanoes: Ongoing ef-
770 forts and perspectives. *Journal of Volcanology and Geothermal Research*, *321*,
771 182–195. doi: 10.1016/j.jvolgeores.2016.04.036
- 772 Brenguier, F., Shapiro, N. M., Campillo, M., Ferrazzini, V., Duputel, Z., Coutant,
773 O., & Nercessian, A. (2008). Towards forecasting volcanic eruptions using
774 seismic noise. *Nature Geoscience*, *1*(2), 126–130. doi: 10.1038/ngeo104
- 775 Budi-Santoso, A., & Lesage, P. (2016). Velocity variations associated with the large
776 2010 eruption of Merapi volcano, Java, retrieved from seismic multiplets and
777 ambient noise cross-correlation. *Geophysical Journal International*, *206*(1),
778 221–240. doi: 10.1093/gji/ggw145
- 779 Chaput, J., Campillo, M., Aster, R. C., Roux, P., Kyle, P. R., Knox, H., & Czoski,
780 P. (2015). Multiple scattering from icequakes at Erebus volcano, Antarc-
781 tica: Implications for imaging at glaciated volcanoes. *Journal of Geophysical*
782 *Research: Solid Earth*, *120*(2), 1129–1141. doi: 10.1002/2014JB011278
- 783 Colombi, A., Chaput, J., Brenguier, F., Hillers, G., Roux, P., & Campillo, M.
784 (2014). On the temporal stability of the coda of ambient noise correla-
785 tions. *Comptes Rendus - Geoscience*, *346*(11-12), 307–316. doi: 10.1016/

786 j.crte.2014.10.002

- 787 Donaldson, C., Caudron, C., Green, R. G., Thelen, W. A., & White, R. S. (2017).
 788 Relative seismic velocity variations correlate with deformation at Klauewa vol-
 789 cano. *Science Advances*, *3*(6), e1700219. doi: 10.1126/sciadv.1700219
- 790 Durbin, J., & Koopman, S. J. (2012). *Time Series Analysis by State Space Methods*
 791 (Second ed.). Oxford University Press. doi: 10.1093/acprof:oso/9780199641178
 792 .001.0001
- 793 Farr, T. G., Rosen, P. A., Caro, E., Crippen, R., Duren, R., Hensley, S., ... Alsdorf,
 794 D. (2007). The Shuttle Radar Topography Mission. *Review of Geophysics*,
 795 *45*(2), RG2004. doi: 10.1029/2005RG000183
- 796 Gassenmeier, M., Sens-Schönfelder, C., Eulendorf, T., Bartsch, M., Victor, P.,
 797 Tilmann, F., & Korn, M. (2016). Field observations of seismic velocity
 798 changes caused by shaking-induced damage and healing due to mesoscopic
 799 nonlinearity. *Geophysical Journal International*, *204*(3), 1490–1502. doi:
 800 10.1093/gji/ggv529
- 801 Gomberg, J., & Agnew, D. (1996). The accuracy of seismic estimates of dynamic
 802 strains: An evaluation using strainmeter and seismometer data from Piñon
 803 Flat Observatory, California. *Bulletin of the Seismological Society of America*,
 804 *86*(1 SUPPL. A), 212–220.
- 805 Hendriyana, A., & Tsuji, T. (2019). Migration of Very Long Period Seismicity at
 806 Aso Volcano, Japan, Associated With the 2016 Kumamoto Earthquake. *Geo-*
 807 *physical Research Letters*, *46*(15), 8763–8771. doi: 10.1029/2019GL082645
- 808 Hillers, G., Ben-Zion, Y., Campillo, M., & Zigone, D. (2015). Seasonal varia-
 809 tions of seismic velocities in the San Jacinto fault area observed with ambient
 810 seismic noise. *Geophysical Journal International*, *202*(2), 920–932. doi:
 811 10.1093/gji/ggv151
- 812 Hillers, G., Husen, S., Obermann, A., Planès, T., Larose, E., & Campillo, M. (2015).
 813 Noise-based monitoring and imaging of aseismic transient deformation induced
 814 by the 2006 Basel reservoir stimulation. *Geophysics*, *80*(4), KS51–KS68. doi:
 815 10.1190/geo2014-0455.1
- 816 Hobiger, M., Wegler, U., Shiomi, K., & Nakahara, H. (2016). Coseismic and post-
 817 seismic velocity changes detected by passive image interferometry: Comparison
 818 of one great and five strong earthquakes in Japan. *Geophysical Journal Inter-*
 819 *national*, *205*(2), 1053–1073. doi: 10.1093/gji/ggw066
- 820 Ichihara, M., & Matsumoto, S. (2017). Relative Source Locations of Contin-
 821 uous Tremor Before and After the Subplinian Events at Shinmoe-dake,
 822 in 2011. *Geophysical Research Letters*, *44*(21), 10,871–10,877. doi:
 823 10.1002/2017GL075293
- 824 Kagiya, T., Utada, H., Uyeshima, M., Masutani, F., Kanda, W., Tanaka, Y., ...
 825 Mishina, M. (1996). Resistivity Structure of the Central and the Southeastern
 826 Part of Kirishima Volcanoes. *Bulltin of the volcanological society of Japan*,
 827 *41*(5), 215–225. doi: 10.18940/kazan.41.5.215
- 828 Kaneshima, S., Kawakatsu, H., Matsubayashi, H., Sudo, Y., Tsutsui, T., Ohminato,
 829 T., ... Idaka, T. (1996). Mechanism of Phreatic Eruptions at Aso Volcano
 830 Inferred from Near-Field Broadband Seismic Observations. *Science*, *273*(5275),
 831 643–645. doi: 10.1126/science.273.5275.643
- 832 Kato, A., Nakamura, K., & Hiyama, Y. (2016). The 2016 Kumamoto earthquake
 833 sequence. *Proceedings of the Japan Academy Series B: Physical and Biological*
 834 *Sciences*, *92*(8), 358–371. doi: 10.2183/pjab.92.359
- 835 Kim, D., & Lekic, V. (2019). Groundwater Variations From Autocorrelation and
 836 Receiver Functions. *Geophysical Research Letters*, *722*–729. doi: 10.1029/
 837 2019GL084719
- 838 Kozono, T., Ueda, H., Ozawa, T., Koyaguchi, T., Fujita, E., Tomiya, A., & Suzuki,
 839 Y. J. (2013). Magma discharge variations during the 2011 eruptions of
 840 Shinmoe-dake volcano, Japan, revealed by geodetic and satellite observations.

- 841 *Bull. Volcanol.*, 75(3), 1–13. doi: 10.1007/s00445-013-0695-4
- 842 Krischer, L., Megies, T., Barsch, R., Beyreuther, M., Lecocq, T., Caudron, C., &
843 Wassermann, J. (2015). ObsPy: A bridge for seismology into the scientific
844 Python ecosystem. *Computational Science and Discovery*, 8(1). doi:
845 10.1088/1749-4699/8/1/014003
- 846 Kurihara, R., Obara, K., Takeo, A., & Tanaka, Y. (2019). Deep Low-Frequency
847 Earthquakes Associated With the Eruptions of Shinmoe-dake in Kirishima Vol-
848 canoes. *Journal of Geophysical Research: Solid Earth*, 2019JB018032. doi:
849 10.1029/2019JB018032
- 850 Lecocq, T., Longuevergne, L., Pedersen, H. A., Brenguier, F., & Stammer, K.
851 (2017). Monitoring ground water storage at mesoscale using seismic noise:
852 30 years of continuous observation and thermo-elastic and hydrological model-
853 ing. *Sci. Rep.*, 7(1), 1–16. doi: 10.1038/s41598-017-14468-9
- 854 Machacca, R., Lesage, P., Larose, E., Lacroix, P., & Anccasi, R. (2019). De-
855 tection of pre-eruptive seismic velocity variations at an andesitic volcano
856 using ambient noise correlation on 3-component stations: Ubinas vol-
857 cano, Peru, 2014. *Journal of Volcanology and Geothermal Research*. doi:
858 10.1016/j.jvolgeores.2019.05.014
- 859 Maeda, T., Obara, K., Furumura, T., & Saito, T. (2011). Interference of long-period
860 seismic wavefield observed by dense hi-net array in japan. *Journal of Geophys-
861 ical Research*, 116.
- 862 Malinverno, A., & Briggs, V. A. (2004). Expanded uncertainty quantification in
863 inverse problems: Hierarchical Bayes and empirical Bayes. *Geophysics*, 69(4),
864 1005–1016. doi: 10.1190/1.1778243
- 865 Miyazawa, M. (2011). Propagation of an earthquake triggering front from the 2011
866 Tohoku-Oki earthquake. *Geophysical Research Letters*, 38(23), n/a–n/a. doi:
867 10.1029/2011GL049795
- 868 Nagaoka, Y. (2020). *Study on seismic velocity structure beneath active volcanoes by
869 seismic interferometry* (PhD). The university of Tokyo.
- 870 Nagaoka, Y., Nishida, K., Aoki, Y., & Takeo, M. (2010). Temporal change of phase
871 velocity beneath Mt. Asama, Japan, inferred from coda wave interferometry.
872 *Geophysical Research Letters*, 37(22), 1–5. doi: 10.1029/2010GL045289
- 873 Nakada, S., Nagai, M., Kaneko, T., Suzuki, Y., & Maeno, F. (2013). The outline
874 of the 2011 eruption at Shinmoe-dake (Kirishima), Japan. *Earth, Planets and
875 Space*, 65(6), 475–488. doi: 10.5047/eps.2013.03.016
- 876 Nakamichi, H., Yamanaka, Y., Terakawa, T., Horikawa, S., Okuda, T., & Ya-
877 mazaki, F. (2013). Continuous long-term array analysis of seismic records
878 observed during the 2011 Shinmoedake eruption activity of Kirishima vol-
879 cano, southwest Japan. *Earth, Planets and Space*, 65(6), 551–562. doi:
880 10.5047/eps.2013.03.002
- 881 Nakao, S., Morita, Y., Yakiwara, H., Oikawa, J., Ueda, H., Takahashi, H., . . . Iguchi,
882 M. (2013). Volume change of the magma reservoir relating to the 2011
883 Kirishima Shinmoe-dake eruption—Charging, discharging and recharging
884 process inferred from GPS measurements. *Earth, Planets and Space*, 65(6),
885 505–515. doi: 10.5047/eps.2013.05.017
- 886 Nimiya, H., Ikeda, T., & Tsuji, T. (2017). Spatial and temporal seismic velocity
887 changes on Kyushu Island during the 2016 Kumamoto earthquake. *Science Ad-
888 vances*, 3(11), e1700813. doi: 10.1126/sciadv.1700813
- 889 Nishida, K., Kawakatsu, H., & Obara, K. (2008). Three-dimensional crustal S wave
890 velocity structure in Japan using microseismic data recorded by Hi-net tilt-
891 meters. *Journal of Geophysical Research: Solid Earth*, 113(B10), B10302. doi:
892 10.1029/2007JB005395
- 893 Niu, F., Silver, P. G., Daley, T. M., Cheng, X., & Majer, E. L. (2008). Preseismic
894 velocity changes observed from active source monitoring at the parkfield safod
895 drill site. *Nature*, 454(7201), 204.

- 896 Obermann, A., & Hillers, G. (2019). Chapter Two - Seismic time-lapse interferom-
 897 etry across scales. In C. Schmelzbach (Ed.), *Advances in seismology* (Vol. 60,
 898 pp. 65–143). Elsevier. doi: 10.1016/bs.agph.2019.06.001
- 899 Obermann, A., Planes, T., Larose, E., Sens-Schönfelder, C., & Campillo, M. (2013).
 900 Depth sensitivity of seismic coda waves to velocity perturbations in an elastic
 901 heterogeneous medium. *Geophysical Journal International*, *194*(1), 372–382.
 902 doi: 10.1093/gji/ggt043
- 903 Ogiso, M., Yomogida, K., & Katsumata, K. (2005). Recursive travel-time inver-
 904 sion: A tool for real-time seismic tomography. *Earth, Planets Sp.*, *57*(6), 477–
 905 489. doi: 10.1186/BF03352582
- 906 Okada, Y. (1992). Internal deformation due to shear and tensile faults in a half-
 907 space. *Bulletin - Seismological Society of America*, *82*(2), 1018–1040.
- 908 Olivier, G., Brenguier, F., Carey, R., Okubo, P., & Donaldson, C. (2019). Decrease
 909 in Seismic Velocity Observed Prior to the 2018 Eruption of Kilauea Volcano
 910 With Ambient Seismic Noise Interferometry. *Geophysical Research Letters*,
 911 *46*(7), 3734–3744. doi: 10.1029/2018GL081609
- 912 Pacheco, C., & Snieder, R. (2005). Time-lapse travel time change of multiply
 913 scattered acoustic waves. *The Journal of the Acoustical Society of America*,
 914 *118*(3), 1300–1310. doi: 10.1121/1.2000827
- 915 Poupinet, G., Ellsworth, W., & Frechet, J. (1984). Monitoring velocity variations
 916 in the crust using earthquake doublets: An application to the calaveras fault,
 917 california. *Journal of Geophysical Research: Solid Earth*, *89*(B7), 5719–5731.
- 918 Rivet, D., Brenguier, F., & Cappa, F. (2015). Improved detection of preruptive
 919 seismic velocity drops at the Piton de La Fournaise volcano. *Geophysical Re-
 920 search Letters*, 1–8. doi: 10.1002/2015GL064835.Received
- 921 Rivet, D., Campillo, M., Shapiro, N. M., Cruz-Atienza, V., Radiguet, M., Cotte, N.,
 922 & Kostoglodov, V. (2011). Seismic evidence of nonlinear crustal deformation
 923 during a large slow slip event in Mexico. *Geophysical Research Letters*, *38*(8),
 924 3–7. doi: 10.1029/2011GL047151
- 925 Sandanbata, O., Obara, K., Maeda, T., Takagi, R., & Satake, K. (2015). Sudden
 926 changes in the amplitude-frequency distribution of long-period tremors at Aso
 927 volcano, southwest Japan. *Geophysical Research Letters*, *42*(23), 10256–10262.
 928 doi: 10.1002/2015GL066443
- 929 Segall, P., & Matthews, M. (1997). Time dependent inversion of geodetic data.
 930 *Journal of Geophysical Research: Solid Earth*, *102*(B10), 22391–22409. doi: 10
 931 .1029/97JB01795
- 932 Sens-Schönfelder, C., & Eulenfeld, T. (2019). Probing the in situ Elastic Nonlin-
 933 earity of Rocks with Earth Tides and Seismic Noise. *Phys. Rev. Lett.*, *122*(13),
 934 138501. doi: 10.1103/PhysRevLett.122.138501
- 935 Sens-Schönfelder, C., Pomponi, E., & Peltier, A. (2014). Dynamics of Piton de
 936 la Fournaise volcano observed by passive image interferometry with multiple
 937 references. *Journal of Volcanology and Geothermal Research*, *276*, 32–45. doi:
 938 10.1016/j.jvolgeores.2014.02.012
- 939 Sens-Schönfelder, C., & Wegler, U. (2006). Passive image interferometry and sea-
 940 sonal variations of seismic velocities at Merapi Volcano, Indonesia. *Geophysical
 941 Research Letters*, *33*(21), 1–5. doi: 10.1029/2006GL027797
- 942 Shapiro, S. A. (2003). Elastic piezosensitivity of porous and fractured rocks. *Geo-
 943 physics*, *68*(2), 482–486. doi: 10.1190/1.1567215
- 944 Snieder, R., Sens-Schönfelder, C., & Wu, R. (2017). The time dependence of rock
 945 healing as a universal relaxation process, a tutorial. *Geophysical Journal Inter-
 946 national*, *208*(1), 1–9. doi: 10.1093/gji/ggw377
- 947 Suzuki, Y., Yasuda, A., Hokanishi, N., Kaneko, T., Nakada, S., & Fujii, T. (2013).
 948 Syneruptive deep magma transfer and shallow magma remobilization during
 949 the 2011 eruption of Shinmoe-dake, Japan-Constraints from melt inclusions
 950 and phase equilibria experiments. *Journal of Volcanology and Geothermal*

- 951 *Research*, 257, 184–204. doi: 10.1016/j.jvolgeores.2013.03.017
- 952 Takano, T., Nishimura, T., & Nakahara, H. (2017). Seismic velocity changes concentrated at the shallow structure as inferred from correlation analyses of ambient
953 noise during volcano deformation at Izu-Oshima, Japan. *Journal of Geophysical
954 Research: Solid Earth*, 122(8), 6721–6736. doi: 10.1002/2017JB014340
- 955 Takano, T., Nishimura, T., Nakahara, H., Ohta, Y., & Tanaka, S. (2014). Seismic
956 velocity changes caused by the Earth tide: Ambient noise correlation analyses
957 of small-array data. *Geophysical Research Letters*, 41(17), 6131–6136. doi:
958 10.1002/2014GL060690
- 959 Takano, T., Nishimura, T., Nakahara, H., Ueda, H., & Fujita, E. (2019). Sen-
960 sitivity of Seismic Velocity Changes to the Tidal Strain at Different Lapse
961 Times: Data Analyses of a Small Seismic Array at Izu-Oshima Volcano.
962 *Journal of Geophysical Research: Solid Earth*, 124(3), 3011–3023. doi:
963 10.1029/2018JB016235
- 964 Takeo, M., Maehara, Y., Ichihara, M., Ohminato, T., Kamata, R., & Oikawa, J.
965 (2013). Ground deformation cycles in a magma-effusive stage, and sub-Plinian
966 and Vulcanian eruptions at Kirishima volcanoes, Japan. *Journal of Geophysical
967 Research: Solid Earth*, 118(9), 4758–4773. doi: 10.1002/jgrb.50278
- 968 Takeuchi, H., & Saito, M. (1972). Seismology: Surface Waves and Free Oscilla-
969 tions. In B. A. Bolt (Ed.), *Methods in computational physics* (Vol. 11, pp. 217–
970 295). Academic Press, New York.
- 971 Talwani, P., Chen, L., & Gahalaut, K. (2007). Seismogenic permeability, ks. *Journal
972 of Geophysical Research: Solid Earth*, 112(B7).
- 973 Tarantola, A., & Valette, B. (1982). Generalized nonlinear inverse problems solved
974 using the least squares criterion. *Reviews of Geophysics*, 20(2), 219. doi: 10
975 .1029/RG020i002p00219
- 976 Tomatsu, T., Kumagai, H., & Dawson, P. B. (2001). Tomographic inversion
977 of P-wave velocity and Q structures beneath the Kirishima volcanic com-
978 plex, Southern Japan, based on finite difference calculations of complex
979 traveltimes. *Geophysical Journal International*, 146(3), 781–794. doi:
980 10.1046/j.1365-246X.2001.00491.x
- 981 Tsukamoto, K., Aizawa, K., Chiba, K., Kanda, W., Uyeshima, M., Koyama, T., ...
982 Kishita, T. (2018). Three-Dimensional Resistivity Structure of Iwo-Yama Vol-
983 cano, Kirishima Volcanic Complex, Japan: Relationship to Shallow Seismicity,
984 Surface Uplift, and a Small Phreatic Eruption. *Geophysical Research Letters*,
985 45(23), 12,821–12,828. doi: 10.1029/2018GL080202
- 986 Ueda, H., Kozono, T., Fujita, E., Kohno, Y., Nagai, M., Miyagi, Y., & Tanada, T.
987 (2013). Crustal deformation associated with the 2011 Shinmoe-dake eruption
988 as observed by tiltmeters and GPS. *Earth, Planets and Space*, 65(6), 517–525.
989 doi: 10.5047/eps.2013.03.001
- 990 Van Der Walt, S., Colbert, S. C., & Varoquaux, G. (2011). The numpy array: a
991 structure for efficient numerical computation. *Computing in Science & Engi-
992 neering*, 13(2), 22–30.
- 993 Virtanen, P., Gommers, R., Oliphant, T. E., Haberland, M., Reddy, T., Cournapeau,
994 D., ... van Mulbregt, P. (2020, mar). SciPy 1.0: fundamental algorithms
995 for scientific computing in Python. *Nature Methods*, 17(3), 261–272. Re-
996 trieved from <http://www.nature.com/articles/s41592-019-0686-2> doi:
997 10.1038/s41592-019-0686-2
- 998 Wang, Q.-Y., Brenguier, F., Campillo, M., Lecointre, A., Takeda, T., & Aoki,
999 Y. (2017). Seasonal crustal seismic velocity changes throughout Japan.
1000 *Journal of Geophysical Research: Solid Earth*, 122(10), 7987–8002. doi:
1001 10.1002/2017JB014307
- 1002 Wang, Q. Y., Campillo, M., Brenguier, F., Lecointre, A., Takeda, T., & Hashima, A.
1003 (2019). Evidence of Changes of Seismic Properties in the Entire Crust Beneath
1004 Japan After the Mw 9.0, 2011 Tohoku-oki Earthquake. *Journal of Geophysical
1005 Research*

1006 *Research: Solid Earth*, 124(8), 8924–8941. doi: 10.1029/2019JB017803
 1007 Weaver, R., Froment, B., & Campillo, M. (2009). On the correlation of non-
 1008 isotropically distributed ballistic scalar diffuse waves. *The Journal of the*
 1009 *Acoustical Society of America*, 126(4), 1817–26. doi: 10.1121/1.3203359
 1010 Weaver, R., Hadziioannou, C., Larose, E., & Campillo, M. (2011). On the precision
 1011 of noise correlation interferometry. *Geophysical Journal International*, 185(3),
 1012 1384–1392. doi: 10.1111/j.1365-246X.2011.05015.x
 1013 Weaver, R., & Lobkis, O. (2000). Temperature dependence of diffuse field phase. *Ul-*
 1014 *trasonics*, 38(1), 491–494. doi: 10.1016/S0041-624X(99)00047-5
 1015 Wegler, U., Nakahara, H., Sens-Schönfelder, C., Korn, M., & Shiomi, K. (2009).
 1016 Sudden drop of seismic velocity after the 2004 Mw 6.6 mid-Niigata earthquake,
 1017 Japan, observed with Passive Image Interferometry B06305. *Journal of Geo-*
 1018 *physical Research: Solid Earth*, 114(6), 1–11. doi: 10.1029/2008JB005869
 1019 Wegler, U., & Sens-Schönfelder, C. (2007). Fault zone monitoring with passive image
 1020 interferometry. *Geophysical Journal International*, 168(3), 1029–1033.
 1021 Wessel, P., Smith, W. H. F., Scharroo, R., Luis, J., & Wobbe, F. (2013). Generic
 1022 mapping tools: Improved version released. *Eos, Transactions American Geo-*
 1023 *physical Union*, 94(45), 409-410. doi: 10.1002/2013EO450001
 1024 Yamada, T., Ueda, H., Mori, T., & Tanada, T. (2019). Tracing Volcanic Activ-
 1025 ity Chronology from a Multiparameter Dataset at Shinmoedake Volcano
 1026 (Kirishima), Japan. *Journal of Disaster Research*, 14(5), 687–700. doi:
 1027 10.20965/jdr.2019.p0687
 1028 Yamamoto, M., & Sato, H. (2010). Multiple scattering and mode conversion re-
 1029 vealed by an active seismic experiment at Asama volcano, Japan. *Journal of*
 1030 *Geophysical Research: Solid Earth*, 115(7), 1–14. doi: 10.1029/2009JB007109
 1031 Yamamura, K., Sano, O., Utada, H., Takei, Y., Nakao, S., & Fukao, Y. (2003).
 1032 Long-term observation of in situ seismic velocity and attenuation. *Jour-*
 1033 *nal of Geophysical Research: Solid Earth*, 108(B6), 1–15. doi: 10.1029/
 1034 2002JB002005
 1035 Zhu, C., Byrd, R. H., Lu, P., & Nocedal, J. (1994). Fortran subroutines for large-
 1036 scale bound constrained optimization. *ACM Trans Math Softw*, 23(4), 550–
 1037 60.

1038 Appendix A Calculation of the likelihood

1039 For an efficient evaluation of the likelihood defined by equation (32), calculation
 1040 of the determinant of a large matrix \mathbf{F}_t ($N \times N$ matrix) becomes the bottleneck. To re-
 1041 duce the calculations, we rewrote the definition of the likelihood as follows. Since $\mathbf{Z}_t \hat{\mathbf{P}}_{t|t-1} \mathbf{Z}_t^T$
 1042 is the symmetric matrix, it can be diagonalized by the unitary matrix \mathbf{U} as

$$1043 \mathbf{U}^t \mathbf{F}_t \mathbf{U} = \mathbf{\Lambda}, \quad (\text{A1})$$

1044 where the eigen matrix $\mathbf{\Lambda}$ can be written

$$1045 \mathbf{\Lambda} \equiv \begin{pmatrix} \lambda_1 & 0 & 0 & \cdots & 0 \\ 0 & \lambda_2 & 0 & \cdots & 0 \\ 0 & 0 & 0 & \cdots & 0 \\ \vdots & \vdots & \vdots & \ddots & \vdots \\ 0 & 0 & 0 & \cdots & 0 \end{pmatrix}, \quad (\text{A2})$$

1046 Since the rank of $\mathbf{Z}_t \hat{\mathbf{P}}_{t|t-1} \mathbf{Z}_t^T$ is 2, the other $N - 2$ eigen values are zeros.

1047 Then the determinant can be written by

$$1048 \det(\mathbf{F}_t) = \det(\mathbf{U}^T \mathbf{F}_t \mathbf{U}) = \det(\mathbf{\Lambda} + h_0 \mathbf{I}) = (\lambda_1 + h_0)(\lambda_2 + h_0)h_0^{N-2}. \quad (\text{A3})$$

1049 Here we consider the eigen values of $\mathbf{Z}_t \hat{\mathbf{P}}_{t|t-1} \mathbf{Z}_t^T$. For a given eigen vector \mathbf{x}_i for eigen
 1050 value λ_i ,

$$1051 \quad \mathbf{Z}_t \hat{\mathbf{P}}_{t|t-1} \mathbf{Z}_t^T \mathbf{x} = \lambda_i \mathbf{x}_i. \quad (\text{A4})$$

1052 Multiply both sides of each equation by \mathbf{Z}_t

$$1053 \quad \mathbf{Z}_t^T \mathbf{Z}_t \hat{\mathbf{P}}_{t|t-1} \mathbf{Z}_t^T \mathbf{x} = \lambda_i \mathbf{Z}_t^T \mathbf{x}_i. \quad (\text{A5})$$

1054 Since this equation can be interpreted as an eigen value problem for the smaller matrix
 1055 $\mathbf{Z}_t^T \mathbf{Z}_t \hat{\mathbf{P}}_{t|t-1}$ (2×2 matrix), we can obtain these efficiently.